





Faculty of Science and Technology

MASTER'S THESIS

Study program/Specialization: Cybernetics and Signal Processing	Spring semester, 2023 Open / Restricted access
Writers: Casper Cappelen Niluja Mahesan	  (Writer's signatures)
Faculty supervisor(s): Morteza Esmaili	
Thesis title: Assessing Preprocessing Methods and Software Tools for Functional Connectivity Analysis	
Credits: 30p	
Keywords: Functional Connectivity, Human Connectome Project, Functional Magnetic Resonance Imaging (fMRI), Resting-state fMRI (rs-fMRI) Neuroimaging	Pages: 76 + enclosure: 2 Stavanger, 2023-06-15

Abstract

This thesis presents an introductory exploration of the neuroimaging field, focusing on volume-based analysis using functional connectivity. By studying resting state data using the Power et al. atlas, the research aims to uncover patterns and relationships between brain regions, employing a qualitative study design with a single subject.

DPABI Toolbox and Connectome Workbench were used to conduct volume-based functional connectivity analyses. DPABI Toolbox was used to preprocess and perform resting state analysis on the Human Connectome Project (HCP) raw data to produce a functional connectivity matrix. Connectome Workbench was used to create a pipeline for creating a resting state functional connectivity matrix. The resting state analysis was performed on the raw data preprocessed by DPABI and the preprocessed data provided by HCP.

The resting state analyses performed on the same data preprocessed by DPABI yielded visually indistinguishable matrices. The similarity metrics further corroborated this observation, indicating no significant dissimilarities. The application of DPABI for preprocessing and resting state analysis was compared with a self-made pipeline utilizing preprocessed data from the HCP. The resting state analyses yielded two matrices that exhibited noticeable differences in their overall intensities, despite sharing a similar structure. The similarity metrics confirmed these distinctions, as they recorded lower values, indicating a dissimilarity between the matrices.

Acknowledgements

We would like to thank our supervisor Morteza Esmaeili for all of his support and encouragement while we were writing this thesis.

Data were provided [in part] by the Human Connectome Project, WU-Minn Consortium (Principal Investigators: David Van Essen and Kamil Ugurbil; 1U54MH091657) funded by the 16 NIH Institutes and Centers that support the NIH Blueprint for Neuroscience Research; and by the McDonnell Center for Systems Neuroscience at Washington University.

Thank you to Jonathan Power for letting us use his brain atlas images.

Contents

Abstract	ii
Acknowledgements	iii
1 Introduction	1
1.1 Motivation and Problem Description	1
1.2 Related work	2
1.3 Approach	2
1.4 Outline	3
2 Background	5
2.1 Structural Magnetic Resonance Imaging	5
2.2 Functional Magnetic Resonance Imaging	6
2.2.1 Resting-state fMRI	6
2.3 Functional connectivity	7
2.3.1 Seed-Based Functional Connectivity	9
2.4 Atlas	9
2.4.1 Power et al. atlas	9
2.5 Preprocessing	12
2.5.1 Slice-timing correction	12
2.5.2 Realignment	12
2.5.3 Brain extraction/ Skull stripping	13
2.5.4 Coregistration	14
2.5.5 Linear detrending	14
2.5.6 Friston-24 parameter model	15
2.5.7 Nuisance covariate regression	15
2.5.8 Spatial Normalisation	16
2.5.9 Spatial Smoothing	18
2.5.10 Signal filtering: Bandpass	19
2.6 Correlation analysis	19
2.6.1 Pearson correlation coefficients	19
2.6.2 Fisher R-to-Z transform	20
2.7 Metrics	20
2.7.1 Mean Square Error	20

2.7.2	Universal Image Quality Index	21
2.7.3	Structural Similarity Index	22
2.8	File formats used in neuroimaging	24
2.8.1	DICOM	24
2.8.2	NIFTI	25
2.8.3	CIFTI	25
3	Material	27
3.1	Human Connectome Project	27
3.2	Minimal processing pipelines from Human Connectome Project	29
3.2.1	HCP Structural Pipelines	29
3.2.2	HCP Functional Pipelines	29
4	Software	31
4.1	DPABI Matlab Toolbox	31
4.2	Windows Subsystem for Linux	33
4.2.1	FreeSurfer	33
4.2.2	Connectome Workbench	33
5	Method	35
5.1	Overview	35
5.2	DPARSFA	36
5.3	Pipeline when using Connectome Workbench to make functional connectivity matrix	41
5.3.1	Making a dense label file	41
5.3.2	Making a dense time series file	45
5.3.3	Making of parcellated functional connectivity matrix	47
6	Results and Discussion	51
6.1	DPABI	51
6.2	Comparison between DPABI toolbox and Connectome workbench	53
6.3	Comparison between the HCP preprocessed data and our preprocessed data	54
6.4	Metrics	55
6.5	Discussion	56
7	Conclusion	63
A	Poster	65
	Bibliography	67

Chapter 1

Introduction

This chapter will serve as an introduction to this thesis regarding functional connectivity. Firstly the motivation for the project and the problem description will be presented. Related work will then be mentioned, briefly describing projects with similar approaches or goals. The approach to this project will then be presented, as well as an outline for the thesis.

1.1 Motivation and Problem Description

The motivation behind this study is to serve as an introductory resource, providing an overview of the neuroimaging field with a focus on conducting volume-based analysis using functional connectivity in the data. By employing the Power et al. atlas, we aim to investigate the patterns and relationships of brain regions in resting state data. Our study focuses on a single subject, employing a qualitative study design to learn about neuroimaging.

One aspect of our research involves comparing preprocessed data from an external source to our preprocessed data originating from the same raw data. The goal is to determine the potential impact of different preprocessing pipelines on the outcomes. Furthermore, we plan to compare the results of our resting state analysis, conducted using the Connectome Workbench software, with those obtained through the DPABI Toolbox. These comparisons will shed light on the differences in functional connectivity patterns for the subject. Ultimately, our study aims to contribute to a fundamental understanding of functional connectivity and provide rudimentary insights into the analysis methods used in neuroimaging research.

1.2 Related work

In 2022, Kardan et al. conducted a study [1] utilising functional magnetic resonance imaging data from the Baby Connectome Project to evaluate the reliability and distinctiveness of resting-state functional connectivity (rsFC) in infants and toddlers while also predicting age within a sample of individuals aged 8 to 26 months. The researchers identified 11 infant-specific resting-state functional networks and highlighted the greater predictive power of within-network connections compared to between-network connections.

The study conducted by Barch in 2017 [2] aims to explore the relationship between abnormalities in brain circuits and psychiatric disorders. It focuses on employing resting state functional connectivity (rs-fcMRI) in evaluating brain circuits and examines the Human Connectome Project's progress in this field. The study emphasises the importance of these advances in understanding neurological circuit dysfunction in psychopathology, highlighting the characteristics and stability of brain circuits as well as their connection to behaviour.

Power et al.'s article [3] provides an overview of the advancements in MRI technology and their impact on understanding functional brain networks in humans. It focuses on the progression of functional networks spanning infancy to adolescence, utilising resting-state functional connectivity MRI. Traditional techniques' drawbacks are highlighted, and graph theory is introduced as a powerful paradigm for network analysis. It emphasises the importance of considering wider network contexts when studying the development of brain systems.

1.3 Approach

The methods performed in this thesis use MATLAB DPABI toolbox and Connectome Workbench running on Linux to perform volume-based functional connectivity analysis. The goal is to produce a functional connectivity matrix from the data of one subject from the Human Connectome Project dataset. Different metrics will be applied to evaluate the similarity between the connectivity matrices.

Two different methods were applied. One uses raw data, which are being preprocessed in the DPABI toolbox. A resting state analysis of the processed raw data is done in the DPABI toolbox and with Connectome Workbench. The other method consists of using data preprocessed by Human Connectome Project and performing resting state analysis in Connectome Workbench.

1.4 Outline

- **Chapter 2: Background**

This chapter explains some relevant background material for this thesis. It covers some neuroimaging techniques, relevant preprocessing steps, correlation analysis and the neuroimaging formats used in this thesis.

- **Chapter 3: Material**

In this chapter, the data material used in this experiment will be presented and how it was obtained.

- **Chapter 4: Software**

The chapter will cover some information about the software used in this thesis.

- **Chapter 5: Method**

This chapter will describe the method for achieving the thesis goal and provide information on how the preprocessing/analysis pipelines are used/created.

- **Chapter 6: Results and Discussion**

This chapter will present the results, and a discussion about the results and project will be conducted.

- **Chapter 7: Conclusion**

This chapter will contain an overall evaluation of the results and the project.

Chapter 2

Background

This chapter covers the essentials of structural MRI and introduces functional MRI, emphasising basics and resting state functional MRI. It explores functional connectivity, including connectivity matrices and seed-based connectivity. The preprocessing steps for fMRI images are explained, followed by correlation analysis focusing on Pearson correlation and Fisher R-to-Z transform. The chapter concludes with an overview of similarity metrics and an introduction to neuroimaging formats.

2.1 Structural Magnetic Resonance Imaging

There are two types of neuroimaging techniques: structural imaging and functional imaging. Structural imaging is a method for visualising and analysing anatomical aspects of the brain. For identifying brain injuries and anomalies, structural approaches are helpful. Geometric parameters can be quantified, such as the size and volume of a specific structure or the thickness of a cortical region [4].

Structural MRI is a non-invasive method for analysis of the brain anatomy and pathology [5]. MRI generates highly detailed images of the brain. The reason for the higher spatial resolution of MRI is attributed to the use of strong magnetic gradients. Tissues in the grey matter, white matter, and other parts of the brain respond differently to magnetic gradients, separating distinct types of tissues and structures [4].

There are various types of MR sequences available for structural neuroimaging. Two examples of these are T1-weighted and T2-weighted MRI. T1-weighted MRI increases the adipose tissue signal while decreasing the water signal. T2-weighted MRI amplifies the water signal [6]. T1-weighted imaging provides the best contrast between grey matter, white matter and cerebrospinal fluid (CSF). This is why T1-weighted imaging is the most commonly used technique for quantitative MRI studies of brain morphology. T2-weighted

imaging, on the other hand, may be preferred for estimation of the intracranial volume [7]. The intracranial volume is the volume within the skull, including the brain, meninges and CSF [8]. T2-weighted imaging is preferred because the enhanced signal intensity of CSF in this sequence allows for easier quantification of CSF [7].

2.2 Functional Magnetic Resonance Imaging

fMRI is an MRI-based technique that monitors physiological changes in the brain. These physiological changes are associated with cognitive or behavioural activity and involve changes in blood flow and oxygen levels. Because it depends on changes in blood oxygen levels, fMRI indirectly measures brain activity. This change in blood oxygen levels is referred to as the blood oxygen level-dependent (BOLD) response [4].

The BOLD signal reflects the cognitive workload in a specific brain region during a given task. That is, an increased workload corresponds to higher metabolic demand in that region [4]. When neurons become more active, they need more oxygen from red blood cells. They achieve this by expanding the surrounding blood vessels, increasing blood flow. As a result, the oxygen concentration rises when the neurons become more active. Because oxygenated blood produces fewer field disturbances than deoxygenated blood, the neuron signals endure longer. The fMRI detects more oxygen in this region, indicating more brain activity [9].

Commonly implemented fMRI techniques acquire brain activity images while subjects execute given specific tasks. fMRI creates a functional map of brain images that displays brain activity. During an fMRI scan, the patient may receive a task, such as raising an arm or thinking of a specific word or phrase. These tasks stimulate the brain, enabling the fMRI to detect brain activity. fMRI can also detect and reveal brain activity while subjects rest inside the scanner with instructions to relax during the scanning. This technique is called resting-state (rs) fMRI [9].

2.2.1 Resting-state fMRI

rs-fMRI is a technique utilised to analyse regional interaction in brain mapping when a subject is relaxed and does not perform a specific task [10]. This technique is based on spontaneous BOLD signal changes. Data can be collected via a specialized scan where people are directed to rest. Since there are no tasks to be completed, rs-fMRI is particularly appealing for patients who may struggle with task instructions, such as those with neurologic, neurosurgical and psychiatric problems, as well as young patients [11].

2.3 Functional connectivity

There are different kinds of connectivity, such as structural and functional. Structural connectivity describes how different areas of the brain are structurally connected, and functional connectivity describes how different areas of the brain are functionally related [12]. Functional connectivity can show how various brain networks or areas cooperate in carrying out cognitive, sensory, or motor activities and how these networks are affected by neurological and psychiatric illnesses [13]. In this thesis, the focus is on functional connectivity.

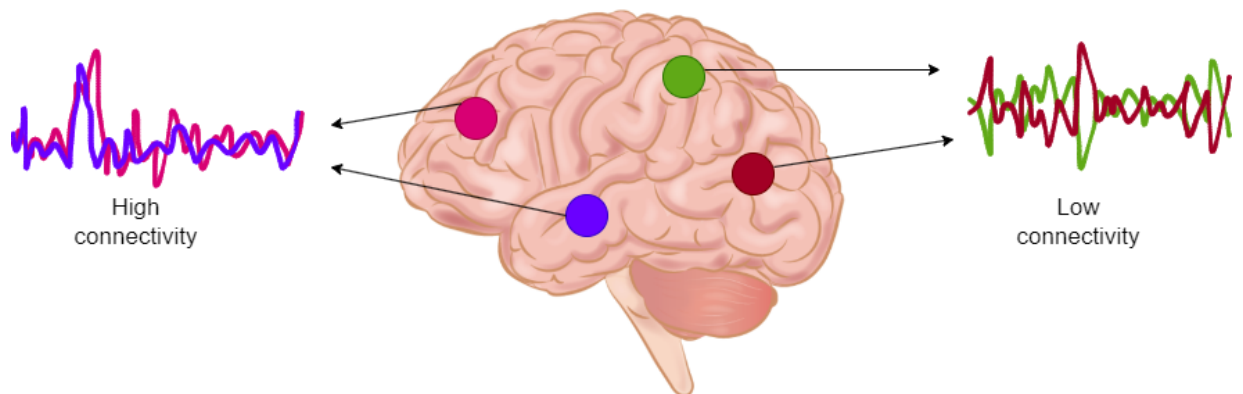


Figure 2.1: The correlation of brain activity between two or more regions of the brain is measured by functional connectivity. The pink and purple regions have a high correlation, while the green and red regions have a low correlation. The brain image is adapted from [14], and the graphs are inspired by Figure 1a, [15].

Functional connectivity (FC) is a term used to describe the statistical relationship or correlation between the activity or communication patterns of various brain regions. In other words, it describes how closely connected or synchronized the activities of various brain regions or networks are [13]. Figure 2.1 illustrates regions of high and low connectivity. The pink and purple signals originate from the pink and purple regions and show similar fluctuations. When overlapped, it can be observed that they look similar and that they are somewhat correlated. These signals form functional connectivity. When the red and green signals are compared, it can be observed that they look less similar and will also have lower correlation [12].

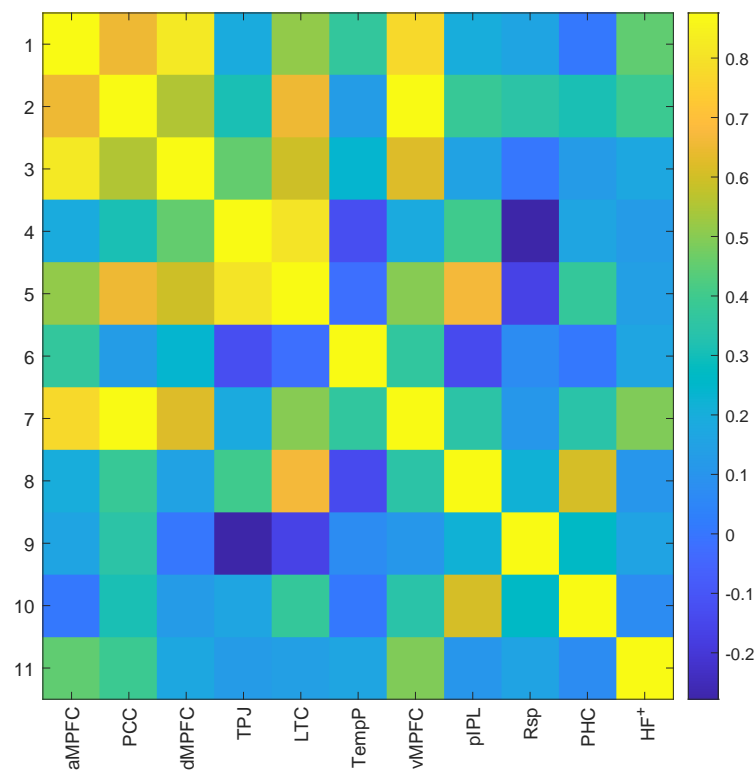


Figure 2.2: An example of a functional connectivity matrix. This is based on DPABI example data with the Hannah-Andrew atlas [16]. The matrix shows that brighter yellow coloured boxes indicate a strong correlation between, for instance, node 7 (vMPFC) and node 2 (PCC). The diagonal line shows a correlation with itself.

Functional connectivity is represented as a matrix which provides a brief but comprehensive description of the pairwise connectivity between all network nodes. In order to construct a connectivity matrix for a brain network consisting of M nodes, it is necessary to generate a two-dimensional square matrix. Each row and column will represent a distinct network node. The elements of this matrix are then filled with the estimated connectivity values for each set of nodes to form an $M \times M$ matrix [17].

Figure 2.2 shows a functional connectivity matrix based on the DPABI example data [18]. The matrix in the figure has an 11×11 matrix because the Hannah-Andrew atlas has 11 nodes. The colour bar to the right shows the relationship between the correlation values and the colours displayed in the matrix. A high correlation or functional connectivity level means the nodes belong to the same system/network. According to [17], the diagonal elements of a functional connectivity matrix can sometimes be interpreted as the representation of each node's connectivity with itself. However, they are used to encode some intrinsic property of each node. The main diagonal in functional connectivity networks may indicate variations in the local dynamics of each region. In practice, the main diagonal is rarely used in neuroscience.

2.3.1 Seed-Based Functional Connectivity

Seed-Based Functional Connectivity Analysis identifies the connectivity between the seeds and the rest of the brain. The seed might be a voxel, a collection of points derived from previous fMRI research, or an atlas. If it is based on an atlas, the seed has a larger region of interest (ROI). The seed-based technique has the benefit of immediately identifying voxel areas to which the seed region is related [19].

Seed-based techniques for functional connectivity analysis require the creation of seed regions. The connectivity map is constructed by extracting time series from each ROI and calculating the correlation between the extracted time series with each other. Seed selection lacks a standardized approach, leaving various alternatives available. [20].

2.4 Atlas

A brain atlas is a collection of maps or templates that provide a standardized representation of the anatomical and functional regions of the brain. Brain atlases are used in neuroimaging studies to identify specific regions, localise functional activity in the brain, and perform spatial normalization of brain images [21].

2.4.1 Power et al. atlas

The Power et al. atlas identifies specific areas of the human brain that co-activate during certain tasks. The default mode network (DMN) is a network of interconnected areas of the brain that are active when a person is relaxed and does not pay attention to a specific task, such as daydreaming or mind-wandering (resting state) [16]. Power et al. atlas is a data-driven methodology based on the functional connectivity patterns within the networks shown in Table 2.1. The atlas identified 264 different areas of the brain that were continuously active during rest periods and functionally related to other networks using fMRI data from a group of healthy adults [22].

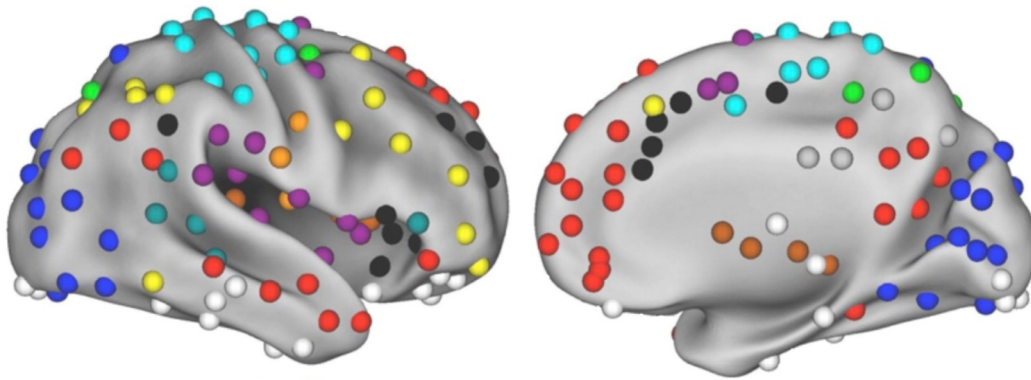















Figure 2.3: The figure shows the 264 nodes divide into different networks [22]. The colours in the atlas correspond to the networks shown in Table 2.1.

The 264 nodes in the atlas were organized into several networks according to their functional connectivity patterns, as shown in Figure 2.3. A small portion of the brain is represented by each node in the Power et al. atlas, and the activity of each node is highly correlated with the activity of the other nodes in the same functional network. These nodes can specify the areas of interest (ROIs) for subsequent analyses [22]. The ROIs are colour-coded according to their system, and Table 2.1 shows the systems and their respective colour.

Table 2.1: The table shows the suggested systems and colours that the ROIs are grouped into in Power et al. atlas [22] and a short description of these systems. The table is constructed using the supplementary Excel spreadsheet from [22].

Suggested Colour		Suggested System	Description
White		Uncertain	Uncertain
Cyan		Sensory/somatomotor Hand	Hand movements [23]
Orange		Sensory/somatomotor Mouth	Mouth movements [23]
Purple		Cingulo-opercular Task Control	Associated with task control, but also involved in a variety of other processes in the cognitive, social, and emotional domains [24]
Pink		Auditory	Auditory
Red		Default mode	Resting state
Gray		Memory retrieval?	Recovery of stored information[25]
Teal		Ventral attention	Involves infrequent or unexpected events that are behaviorally relevant[26]
Blue		Visual	Visual
Yellow		Fronto-parietal Task Control	Participation in a task and mental effort[27]
Black		Salience	Acts as a dynamic switch between the Fronto-parietal and DMN[27]
Brown		Subcortical	Involved in intricate processes like hormone production, memory, emotion, and pleasure[28]
Pale blue		Cerebellar	Involved in motor control[29]
Green		Dorsal attention	Feature-based attention (e.g. when the colour of a target object is precued)[26]

2.5 Preprocessing

The preprocessing of fMRI data varies depending on the software programme and the study. However, a standard range of procedures is available to select from [30]. This section shows different operations and the typical order in which they have been performed. This includes slice-timing correction, realignment, brain extraction, segmentation, coregistration between functional and structural images, nuisance regression to remove some physiological and non-physiological signals, spatial normalisation, spatial smoothing, and bandpass filtering. All the necessary preprocessing steps should be applied before performing any functional connectivity analyses [31].

2.5.1 Slice-timing correction

Precise timing is crucial for the analysis of fMRI data. Datasets are typically measured using repeated 2D imaging techniques, which result in a temporal offset. To avoid this time difference, slice-timing correction is used as an fMRI preprocessing step [32]. This is done by changing the time series of each slice to align them with a reference time point [33], as shown in Figure 2.4.

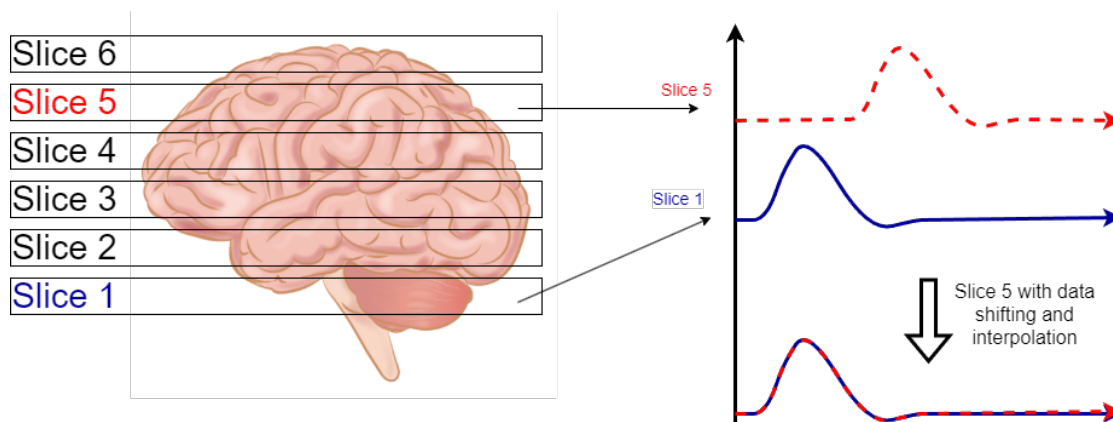


Figure 2.4: Slice-timing correction: To match the starting time, the signal evoked at slice 5 is moved towards slice 1. Then the shifted signal is interpolated [14].

2.5.2 Realignment

The main component that affects the data is head movement. When subjects are in a state of rest, the voxel that corresponds to the signal generated within the brain tissue remains fixed. When the subject moves its head, the signal generated by the same brain tissue will be localized in a voxel different from its initial position. This is a significant issue that is reduced during realignment and ensures that the signal in a certain voxel has the same series of data [34].

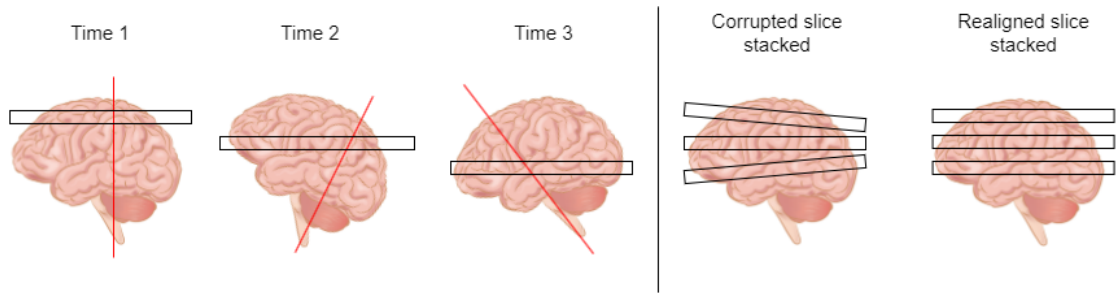


Figure 2.5: The patient moves while the images are being acquired slice by slice, as shown in the figure, leading to a corrupted slice-stacked volume. By applying realignment, the slices will stack in line with each other. The brain image is adapted from [14], and the image is inspired by Figure 5 from [35].

The goal of realignment is to place all the functional images in line with one another such that the brain appears in the same location in each image, as shown in Figure 2.5. Even if the head is stuffed with padding or foam during data gathering, head movement will still be observed. These movements will result in two significant issues. Firstly, the source of the signal within a voxel can change over time and between scans, leading to a fake activation. Secondly, the signal-to-noise ratio (SNR) may be impacted by movement. The purpose of realignment is to guarantee that the source of the signal in a particular voxel is always in the same physical place; however, even after realignment, some artefacts remain. This is still an important step in the preprocessing of fMRI data [34].

2.5.3 Brain extraction/ Skull stripping

Brain extraction, or skull stripping, is commonly performed before brain segmentation. Brain extraction removes non-brain tissue from brain imaging, such as the skull, dura, and scalp. It is also known as brain/non-brain segmentation because the brain predominantly consists of WM, GM, CSF, and the cerebellum [36].

Brain segmentation is a complex problem because of the non-homogeneous intensity distribution found in brain regions and intensity overlap with surrounding non-brain structures. This problem requires advanced algorithms and significant human involvement for parameter adjustment. Although there are numerous brain/non-brain segmentation methods, the majority are time-consuming, laborious, and lack rapid brain visualisation [36].

Frequently, fMRI images consist of little non-brain tissue caused by the nature of the imaging. On the other hand, high-resolution MR images almost always contain a significant amount of eyes, skin, fat, muscle, etc. The robustness of functional image coregistration to high-resolution MR images will be increased if these non-brain components of the images can be automatically discarded prior to coregistration [37].

Brain Extraction Tool (BET) is a fully automated brain extraction tool that has been tested on a variety of MR modalities, such as T1-weighted and T2-weighted [37]. The intensity histogram is processed to determine the image's "robust" lower and upper intensity values, as well as a rough brain/non-brain threshold. The image's centre of gravity is determined, as well as the approximate size of the head [38].

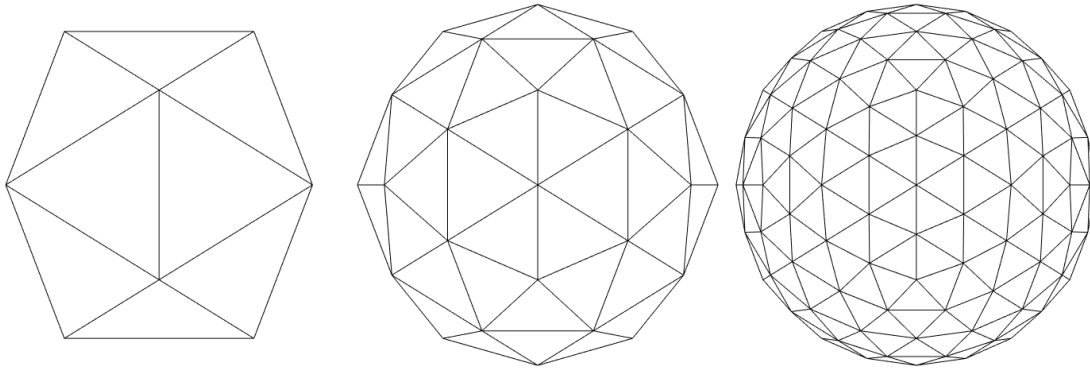


Figure 2.6: This figure shows an illustration of the triangular tessellation of a sphere.

Figure 2.6 illustrates a triangular tessellation of a sphere's surface. A similar tessellation is initiated and gradually deformed inside the brain, one vertex at a time. The deformation happens according to the forces that keep the surface well-spaced and smooth while seeking to migrate towards the edge of the brain. The procedure is restarted with a more significant smoothness constraint if a sufficiently clean solution cannot be identified. Finally, if necessary, the skull's outer surface is calculated [38].

2.5.4 Coregistration

The fundamental coregistration task is to align two 2D or 3D images. In other words, modify one spatially to fit the other. This is accomplished by establishing a connection between the voxel sites in the two images. Once this connection is known, merging the data at the corresponding locations is possible, allowing for the fusion or comparison of the two images. For instance, in functional MRI, the functional, low-resolution activations can be connected to the anatomical structures shown in a separate high-resolution structural image of the same subject [39].

2.5.5 Linear detrending

Temporal variations in scanner magnetic fields or physiological factors can be used to explain the signal drift in fMRI. Given that these variables have an impact on signals in the entire brain, a method for removing spatially global effects of drift has been to regress out or proportionally scale out spatial mean signals from fMRI signals. However,

this method does not consider regional variability in fMRI drifts. One of the most common solutions is to linearly reduce the signal drifts in each voxel, which is called linear detrending [40].

2.5.6 Friston-24 parameter model

fMRI is particularly challenging when it comes to head motion. According to [41], recent research [42–45] has shown that the combined impact of "micro" head movements as small as 0.1 mm between time points can introduce systematic artefactual inter-individual and group-related differences in fMRI metrics. In the article [41], several potential solutions to overcome motion in fMRI data were proposed. The simplest and most obvious option to reduce motion head was using restraint devices (bite bars and vacuum packing) and having pre-scanning practice sessions using MRI simulators. Even if these solutions are successful, they do not increase the ability to utilise the previously obtained data.

The Friston 24-parameter model [46] is an autoregressive model that includes current and previous position parameters, as well as the square of each parameter. This is a regression of realigned data on six head motion parameters, six head motion parameters one-time point before, and 12 corresponding squared items [41]. The six head motion parameters correspond to rigid-body transformation, so the translation in x, y, z direction, and rotations α, β, γ . The Friston 24-parameter model is a method for removing the confounding effects of movement-related artefacts in fMRI time series. This method is based on the assumption that residual motion artefacts remain even after perfect realignment. These artefacts are classified into two parts. The first part is dependent on the absolute position in the image space relative to the scanner. The second part is due to the history of previous displacements or changes in position from scan to scan. In this thesis, only the necessary description of the Friston 24-parameter model has been provided. For the details of this model, read the original paper [46].

2.5.7 Nuisance covariate regression

One of the biggest confounds for fMRI is physiological noise, as it affects the BOLD signals [47]. Physiological noise is defined as image signal fluctuations induced by the subject's physiology but excluding brain activity of relevance. The main source of the physiological noise signals is the respiratory and cardiac systems. These physiological sources of noise give time-varying signals that, if not corrected, can obscure signals of interest [48].

The purpose of nuisance regression is to decrease nuisance term contributions in BOLD time courses [30]. Head motion, a polynomial trend to simulate scanner drift, signals from CSF, WM, and a whole brain global signal (GS) are all nuisance regressors [49].

The addition of mean WM and CSF signals has the purpose of lessening the influence of non-neural BOLD fluctuations produced by motion, scanner artefacts, and physiological signals that are usually uninteresting (e.g., respiration) [50].

The global signal is a time series of signal intensities averaged across all voxels in the brain. The global signal is a nuisance regressor in dynamic rs-fMRI research because it is highly connected to non-neuronal activities like head motion and breathing patterns. The use of global signal regressor (GSR) has caused controversy in the rs-fMRI literature, with concerns that it may remove signals of interest and bias group comparisons [50]. According to [50], recent studies comparing various denoising pipelines on motion artefacts in rs-fMRI show that using GSR in preprocessing pipelines is effective at suppressing the relationship between motion and functional connectivity but might have some unfavourable impact on the distance-dependent effects of motion.

2.5.8 Spatial Normalisation

Spatial normalisation is the process of spatially translating data into a common space for analysis. When planning surgery to remove a tumour, fMRI may be used to gather data from a single person to understand that specific person. Most of the time, however, we want to generalize across people in order to draw conclusions about how the brain works, which is more generally applicable to our species. Individual brains vary greatly in size and shape, requiring transformation of the brains to match them with one another before the data can be combined across individuals [30].

An accurate and reliable spatial normalisation process is essential for the analysis of fMRI data. By comparing each subject to a predefined template, spatial normalisation attempts to build a one-to-one relationship between the brains of various individuals [51]. It helps to correct for individual differences in brain anatomy and to reduce the variability between individuals, which can improve the accuracy and sensitivity [30].

Spatial Normalisation by DARTEL and New Segmentation

DARTEL stands for "Diffeomorphic Anatomical Registration Through Exponentiated Lie algebra" and is an algorithm for diffeomorphic image registration. Image registration involves calculating a smooth continuous mapping between the points in one image and the points in another image. The parameters that encode the mapping can then be used to determine the relative shapes of the images. The goal is usually to find the single "best" set of values for these parameters. There are numerous approaches to modelling such mappings [52].

One approach is the diffeomorphic setting. A diffeomorphic transformation from one image to another can be represented as a vector field, with each vector describing the movement of data in that voxel from the original to the transformed image. The number of parameters in these transformations is very large, but they are regularized to ensure that the deformations are smooth and do not disrupt the overall structure of the transformed objects [30].

The DARTEL algorithm has been found to improve individual registration, and thus, improve localization and sensitivity during analyses. As this method is more deformable, it improves the realignment of smaller inner structures [53].

The DARTEL and its predecessor, Unified Segmentation, are two of the most commonly used normalisation algorithms, both of which are implemented in SPM. Unified Segmentation is an iterative model that combines segmentation, bias correction and spatial normalisation using WM, GM and CSF tissue maps as priors (TPMs). These TPMs are deformed by a linear combination of a thousand cosine transform bases, and the intensity of each tissue class is modelled using several Gaussian distributions [54].

DARTEL requires the segmentation of all subjects in the group to create the average template, whereas Unified Segmentation combines segmentation and normalisation. Aside from Unified Segmentation, the New Segmentation toolbox included with the SPM12 distribution is another option for providing DARTEL with the required GM and WM segmentation. This algorithm is almost identical to the one described in the Unified Segmentation model. New Segmentation may also provide deformation fields, which can then be used to spatially normalise images [54].

The Montreal Neurological Institute

The Montreal Neurological Institute's 152 brain template (MNI-152) is the most widely used template for spatial normalisation in neuroimaging studies. This template was created using high-resolution T1-weighted scans from 152 normal subjects, where 86 of them were men and 66 were women. MNI-152 became the standard template because of its comprehensive coverage of the brain and increased resolution [55].

To develop the MNI-152 brain template, Automated image registration (AIR) algorithms were used to align brain MRI scans with the reference brain image (target image). The AIR algorithm is utilised to align 3D and 2D images within and between subjects and imaging modalities [56]. The brain MRI images were first linearly registered to the target image (through a 9-parameter affine transformation) and then non-linearly registered to account for anatomical changes in shape, size, and relative orientation between subjects. The MNI-152 brain template has the advantage of covering the entire head and providing

more detailed information from the top of the brain to the bottom of the cerebellum. On the other hand, the MNI-152 template lacks cortical details [57].

2.5.9 Spatial Smoothing

Depending on the filter design, smoothing fMRI data before statistical analysis might increase the signal-to-noise ratio (SNR) and sensitivity to signals of certain shapes and sizes. Smoothing is applied before estimating image registration parameters as it improves registration. Smoothing can also assist in eliminating resampling artefacts following image registration. It can also be utilised to mitigate the effects of functional and anatomical variation within and between people. A downside of smoothing is that it can cause a partial-voluming artefact around the boundary of the brain when brain voxels are smoothed with no-brain voxels. Smoothing has additional negative effects, such as a reduction in effective spatial resolution and blurring and/or shifting of activations [58].

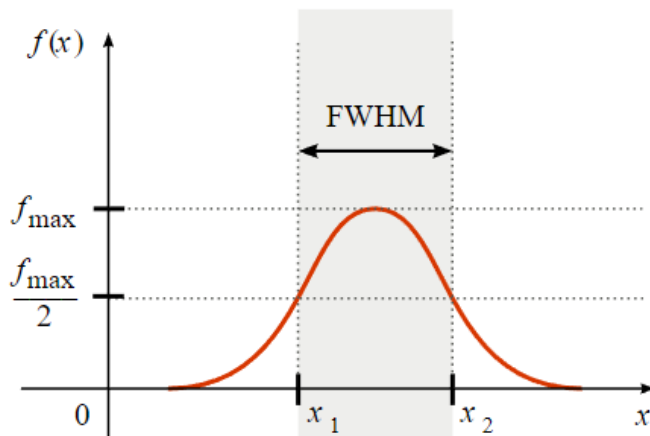


Figure 2.7: The figure shows the definition of FWHM. The x-axis represents the frequency, while the y-axis represents the amplitude. The FWHM is the frequency of the shaded region between the points on the curve where the amplitude is half of its maximum [59].

Convolution of three-dimensional images with a three-dimensional Gaussian filter (or kernel) is the most common method of spatial smoothing. The width of the distribution determines the amount of smoothing imposed by a Gaussian kernel. The standard deviation (σ) is commonly used in statistics to describe this, whereas the full width at half maximum (FWHM) is used in image processing to describe the width of the distribution, as shown in Figure 2.7. This measures the width of the distribution at half its maximum. It is related to the standard deviation by the equation 2.1[30].

$$\text{FWHM} = 2\sigma\sqrt{\ln(2)} \quad (2.1)$$

The bigger the FWHM, the bigger the smoothing. One general rule of thumb is that the Gaussian smoothing kernel should be approximately 2-3 times the voxel size [60].

2.5.10 Signal filtering: Bandpass

The majority of the research on resting state functional networks has concentrated on low frequencies, typically around 0.01-0.1 Hz for BOLD signals [61]. If a higher frequency band is included, the signal may be contaminated by physiological signals [62]. For instance, 0.15–0.25 Hz corresponds to the respiratory frequency range [63]. Frequencies under 0.01 Hz are mostly related to non-physiologic sources like MR scanner drift [64].

2.6 Correlation analysis

Correlation analyses are attempts to find how closely two variables are related. The main goal of correlation analyses is to establish the presence of a relationship between variables, as well as to quantify and characterize that relationship [65].

2.6.1 Pearson correlation coefficients

The Pearson correlation coefficient is one of the most common statistical methods used to estimate functional connectivity. Equation 2.2 shows the formula for Pearson correlation [66].

$$r = \frac{\sum_{i=1}^n (X_i - \bar{X})(Y_i - \bar{Y})}{\sqrt{\sum_{i=1}^n (X_i - \bar{X})^2} \sqrt{\sum_{i=1}^n (Y_i - \bar{Y})^2}} \quad (2.2)$$

In Equation 2.2, n indicates the number of time points. X and Y represent the time series of the brain activity and \bar{X} and \bar{Y} are the means of the time series [66].

The functional connectivity is determined by using the Pearson correlation between BOLD time series from pairs of brain regions (ROIs). The method measures the linear relationship between two variables [67]. The sampling distribution for highly correlated variables is highly skewed. Figure 2.8 shows an illustration of symmetrical distribution, negative, and positive skew. This skew occurs because the correlation is constrained to the interval $[-1,1]$ [68].

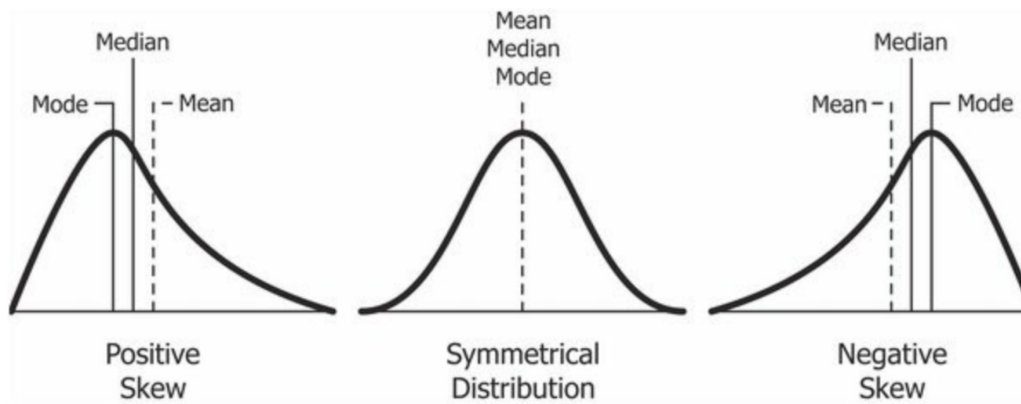


Figure 2.8: The figure shows the different skew distributions [69].

2.6.2 Fisher R-to-Z transform

Most analyses also involve the Fisher R-to-Z transform, where R is the Pearson correlation coefficient and Z is the normal distribution. Fisher's z-transform of the resulting Pearson correlation transforms the skewed sample correlation (R) distribution into one that resembles a normal distribution. The transformation expands the dynamic range beyond [-1,1]. When examining changes in functional connectivity, this is crucial because eliminating the Fisher R-to-Z transform would artificially constrain the dynamics of the data. Fisher's z-transform is shown in Equation 2.3 [66].

$$Fz = \operatorname{atanh}(r) \quad (2.3)$$

2.7 Metrics

2.7.1 Mean Square Error

The mean squared error (MSE) is the average squared difference between the values observed in a study and the values predicted by a model. The differences must be squared because some data values will be greater than the prediction, while other data values will be smaller. Thus their differences can be either positive or negative. Given that observations can be greater than or less than predicted values, the differences can add up to zero. This situation is eliminated by squaring these differences [70].

$$MSE = \frac{\sum_{i=1}^N (y_i - \hat{y}_i)^2}{N} \quad (2.4)$$

Equation 2.4 shows the formula for MSE, where N is the number of observations, y_i is the observed data, and \hat{y}_i is the predicted data [71].

Squaring the differences removes negative difference values and ensures that the mean squared error is always greater than or equal to zero. Only a perfect model with no errors can give an MSE of zero. In practice, it does not occur [71].

2.7.2 Universal Image Quality Index

The universal image quality index (UQI) is a mathematically defined quality index based on the statistical properties of the images in comparison. Wang describes the quality index as universal since the measurement approach is independent of the tested images, the viewing conditions or the observer. The UQI is defined as Equation 2.5, with the definitions of the different values found in Table 2.2 [72].

$$Q = \frac{4\sigma_{xy}\bar{x}\bar{y}}{(\sigma_x^2 + \sigma_y^2)[(\bar{x})^2 + (\bar{y})^2]} \quad (2.5)$$

Table 2.2: Variable Definitions for UQI [72].

Variable	Definition
Q	Image quality index
\mathbf{x}	Original image
\mathbf{y}	Test image
\bar{x}, \bar{y}	Mean of original and test image
σ_x^2, σ_y^2	Variance of original and test image
σ_{xy}	Covariance between original and test image

The value of the quality factor Q has a range of $[-1, 1]$. The best quality factor of 1 is obtained if, and only if, $x_i = y_i$ for all pixels. The lowest value of -1 is obtained if $y_i = 2\bar{x} - x_i$ for all pixels. The quality index measures distortion between two images based on loss of correlation, luminance, and contrast distortion. It is not easy to see this from Equation 2.5, so the Q index is rewritten to Equation 2.6, with variable definitions found in Table 2.2 [72].

$$Q = \underbrace{\frac{\sigma_{xy}}{\sigma_x\sigma_y}}_{\text{Correlation}} \cdot \underbrace{\frac{2\bar{x}\bar{y}}{(\bar{x})^2 + (\bar{y})^2}}_{\text{Luminance}} \cdot \underbrace{\frac{2\sigma_x\sigma_y}{(\sigma_x^2 + \sigma_y^2)}}_{\text{Contrast}} \quad (2.6)$$

Equation 2.6 **Correlation** measures the linear correlation between image \mathbf{x} and \mathbf{y} . The dynamic range for this part of the equation is $[-1, 1]$. The highest correlation coefficient of 1 is obtained when $y_i = ax_i + b$ for all pixels, i , while $a > 0$. To measure relative distortions between \mathbf{x} and \mathbf{y} , the luminance and contrast are compared between \mathbf{x} and

\mathbf{y} . Equation 2.6 **Luminance** measures how close the mean luminance is between \mathbf{x} and \mathbf{y} . The factor has a range between $[0, 1]$ and 1 is obtainable only if $\bar{x} = \bar{y}$. Equation 2.6 **Contrast** compares how close the contrasts are of the two images, where σ_x and σ_y can be viewed as estimates of the contrast of \mathbf{x} and \mathbf{y} [72].

In general, images are non-stationary, as can the image quality be. Even if the image quality is space variant, it is often preferable to have a single evaluation of the overall quality of the image. It is therefore proposed in [72] that an appropriate way to evaluate the image quality is through local measurement of the statistical features and then combining them to an overall image quality factor. The proposed method by Wang and Bovik is a sliding window method with a window size of $B \times B$ pixels. The sliding window is moved horizontally and vertically pixel by pixel, starting from the top left corner until the bottom right corner is reached. There will be M amount of steps when the bottom right corner is reached. The overall quality factor is computed as a mean of locally computed quality factors Q_j , as shown in equation 2.7.

$$Q = \frac{1}{M} \sum_{j=1}^M Q_j \quad (2.7)$$

2.7.3 Structural Similarity Index

The Structural similarity index (SSIM) is an image quality metric algorithm proposed by Wang et al. in 2004 [73]. The luminance of each of the images in question is first compared. The luminance comparison function is defined as $l(\mathbf{x}, \mathbf{y})$, where \mathbf{x} and \mathbf{y} are the images being compared. $l(\mathbf{x}, \mathbf{y})$ will be a function of μ_x and μ_y . The standard deviation σ_x and σ_y are used as an estimate of the contrast and used in the contrast comparison $c(\mathbf{x}, \mathbf{y})$. The structural comparison $s(\mathbf{x}, \mathbf{y})$ is normalised, so demeaned and divided by the standard deviations. These signals are combined in a function yielding the overall similarity measure given in Equation 2.8.

$$S(\mathbf{x}, \mathbf{y}) = f(l(\mathbf{x}, \mathbf{y}), c(\mathbf{x}, \mathbf{y}), s(\mathbf{x}, \mathbf{y})) \quad (2.8)$$

Equation 2.8 is the general form of the comparison metric $S(\mathbf{x}, \mathbf{y})$. The following list describes a set of conditions for the similarity metric that should be satisfied by choice of $l(\mathbf{x}, \mathbf{y})$, $c(\mathbf{x}, \mathbf{y})$ and $s(\mathbf{x}, \mathbf{y})$.

1. Symmetry: $S(\mathbf{x}, \mathbf{y}) = S(\mathbf{y}, \mathbf{x})$
2. Boundedness: $S(\mathbf{x}, \mathbf{y}) \leq 1$

3. Unique maximum: $S(\mathbf{x}, \mathbf{y}) = 1$ if and only if $\mathbf{x} = \mathbf{y}$

Equations 2.9-2.11 are the proposed equations for luminance, contrast and structure comparisons.

$$l(\mathbf{x}, \mathbf{y}) = \frac{2\mu_x\mu_y + C_1}{\mu_x^2 + \mu_y^2 + C_1} \quad (2.9)$$

$$c(\mathbf{x}, \mathbf{y}) = \frac{2\sigma_x\sigma_y + C_2}{\sigma_x^2 + \sigma_y^2 + C_2} \quad (2.10)$$

$$s(\mathbf{x}, \mathbf{y}) = \frac{\sigma_{xy} + C_3}{\sigma_x\sigma_y + C_3} \quad (2.11)$$

The constants C_1 , C_2 and C_3 are defined in Equations 2.12-2.14, where L is defined as the dynamic range of the pixel values (255 for 8-bit greyscale images). K_1 and K_2 are defined as much smaller than 1.

$$C_1 = (K_1L)^2 \quad (2.12)$$

$$C_2 = (K_2L)^2 \quad (2.13)$$

$$C_3 = \frac{C_2}{2} \quad (2.14)$$

The Comparison equations 2.9-2.11 are then combined into SSIM in Equation 2.15. α , β and γ are weighing factors to determine the importance of each comparison component. If $C_1 = C_2 = 0$ and $\alpha = \beta = \gamma = 1$, then SSIM is the same as UQI. SSIM can therefore be viewed as a generalisation of UQI [73].

$$\text{SSIM}(\mathbf{x}, \mathbf{y}) = [l(\mathbf{x}, \mathbf{y})]^\alpha \cdot [c(\mathbf{x}, \mathbf{y})]^\beta \cdot [s(\mathbf{x}, \mathbf{y})]^\gamma \quad (2.15)$$

SSIM is calculated using a sliding window, but instead of a square window, an 11×11 circular Gaussian weighing function is used with a standard deviation of 1.5 samples. In the paper, $\alpha = \beta = \gamma = 1$ and $C_3 = C_2/2$ for simplicity. Wang et al. also used $K_1 = 0.01$ and $K_2 = 0.03$, then noted that K_1 and K_2 values are somewhat arbitrary and insensitive to variation of the values [73].

With the defined values of α, β, γ and $C_1 - C_3$, Equation 2.15 simplifies to 2.16, which is used in calculation [73].

$$\text{SSIM}(\mathbf{x}, \mathbf{y}) = \frac{(2\mu_x\mu_y + C_1)(2\sigma_{xy} + C_2)}{(\mu_x^2 + \mu_y^2 + C_1)(\sigma_x^2 + \sigma_y^2 + C_2)} \quad (2.16)$$

2.8 File formats used in neuroimaging

The datasets used in neuroscience are often complex and large. They consist of many images and metadata for particular types of scans. Data from fMRI scans can be saved in either NIFTI or DICOM formats according to Moore et al. [74]. In addition to these formats, the CIFTI format exists. There are different reasons to use the different formats explained in this section.

2.8.1 DICOM

DICOM (Digital Imaging and Communication in Medicine) is a complex image format designed for use and support in a wide range of medical imaging and clinical procedures. Computed tomography (CT), MRI, ultrasound, x-ray angiography, mammography, and radiation therapy are among the imaging modalities supported. Most equipment directly exports images to the DICOM file format with a .dcm extension. It is also possible to use another form of DICOM with an alternate extension [74].

An advantage of DICOM files is that the medical images are not separated from the key information about their creation. To accomplish this, the image pixel data is grouped with a header of important parameters about the patient, study and the image. Some of the parameters regarding the patient are name, age and sex of the patient. The parameters regarding the study include the physician, study date, and modality, but are not limited to these parameters. The name of the device, the manufacturer, and scanner settings are some of the parameters represented for the imaging details.

The complex and comprehensive nature of the format, DICOM files and datasets can be a burden to store due to the large required storage space. In addition to the resources required, each DICOM file contains the encoding of a single 2D slice instead of a 3D image. This results in many separate files to manage while working with 3D images. It is, therefore, beneficial for neurological scientists to convert DICOM files to a comparatively simpler NIFTI format for better support regarding analysis and visualisation [74].

2.8.2 NIFTI

NIFTI (Neuroimaging Informatics Technology Initiative) is a file format developed by the National Institute of Health in the early 2000s and is a format specifically for neuroimaging. It is built upon a previously-used format called ANALYZE and made improvements such as increased information storage for avoiding ambiguous interpretation and additional datatype support compared to ANALYZE. The NIFTI format contains a header and uncompressed image data. The image data can be stored as separate files, such as `.hdr` and `.img` file formats for header and images, respectively, or as a combined file as `.nii` or `.nii.gz`. The `.nii` extension means that the data is uncompressed, and `.nii.gz` means that the data is compressed. The image data is in contrast to DICOM stored as a 3D matrix, making NIFTI capable of storing volume data. The NIFTI header is a list containing technical parameters such as data scaling, slicing details, axis information and some fields for a brief description and naming [74].

There are two types of the NIFTI format, NIFTI-1 and NIFTI-2. According to Mark Jenkinson on the NITRC forum [75], the NIFTI-2 format is a 64-bit update of NIFTI-1. The intention of NIFTI-2 is to enable the storage of large images and matrices. All dimensions are coded by 64-bit rather than the 16-bit signed integers of NIFTI-1. Even though it is a different format, it will still retain the same naming and formatting of `.nii/.nii.gz` or `.hdr/.img`. It is worth noting that NIFTI-1 and NIFTI-2 are not bitwise compatible with each other [74].

2.8.3 CIFTI

The CIFTI-1 format is a file format that was developed to manage data files relating to brain connectivity and function employing modalities such as fMRI, diffusion MRI, and tractography. The listed modalities have large files and need a format that can handle the large files. The format must also be able to incorporate data representations that reflect components of brain geometry and circuitry. CIFTI-1 files use NIFTI-2 files as a basis but include extra information that allows surface data to be provided in the same format. Vertices are used to represent surface data, whereas voxels are used to represent volume data. Together these are referred to as brainordinates (from brain coordinates [76]). Due to several restrictions in the CIFTI-1 format, Coalson et al. created the CIFTI-2 format, which is detailed in [77]. CIFTI-2 is not backwards compatible with CIFTI-1, although it is possible to convert from CIFTI-1 to CIFTI-2.

CIFTI files consist of two main parts. They consist of a matrix of values and the CIFTI XML as a description of how the matrix indices should be interpreted [77]. Index in this setting is defined as an integer starting from zero that indicates the position along one

dimension of the matrix. In the documentation for CIFTI-2 [77], Coalson et al. describe that there are several different mapping types for each dimension. They use "series" as an example of a straightforward mapping type described as regularly spaced samples. "Brain models" are an example of a more complicated mapping type. They can include vertices from one or more surfaces and specific groupings of voxels. A two-dimensional matrix may hold time series data for surfaces and voxels by mapping indices along one dimension with a "brain models" mapping and indices along the other dimension with a "series" mapping. The brain model element for mapping the matrix indices to voxels or vertices contains a set of attributes, including BrainStructure. This attribute is used to identify the brain structure. Within the brain models index, there are one or more brain structures with each voxel/vertice to create the brainordinates. Table 2.3 shows examples of the different brain structures that can be assigned. The complete list can be found in [77].

Table 2.3: An excerpt of the full list of brain structures used in the BrainModel element of the CIFTI format. Full list in [77] page 10 under the list title BrainStructure Values.

Brain Structure
CIFTI_STRUCTURE_CORTEX
CIFTI_STRUCTURE_CORTEX_LEFT
CIFTI_STRUCTURE_CORTEX_RIGHT
CIFTI_STRUCTURE_OTHER

Data files on the CIFTI format have the additional information about the matrix indices encoded in XML, a markup language that lets the user define and store data in a sharable manner [78]. The CIFTI-2 files have this XML placed into a header extension in a NIFTI-2 file. CIFTI-2 files have a two-part filename extension to distinguish between different CIFTI files. Some examples of these extensions are .dlabel (dense label), .dtseries (dense data series), .ptseries (parcellated data series), and .pconn (parcellated connectivity) [77], which will be used in this project.

Chapter 3

Material

The Connectome Coordination Facility (CCF) manages and distributes public research data for several studies focusing on the connections within the human brain. These are referred to as Human Connectome Projects [79].

3.1 Human Connectome Project

The Human Connectome Project (HCP) was a scientific project that attempts to understand how neural networks or connectomes of the human brain are organized. The HCP aimed to collect and distribute information about the structural and functional connectivity of the human brain. Through brain imaging techniques, researchers have collected information from thousands of participants to examine the complex wiring of the brain. To better understand how genetics and the environment affect brain connectivity, researchers collected DNA, demographic data, and behavioural data from the participants [80].

The HCP dataset includes neuroimaging data from around 1200 healthy young adults. By providing information on brain connectivity and its relationships with behaviour, it is possible to deepen the understanding of how the environment and genes affect changes in the brain circuitry [80]. The 1200 Subjects Release (S1200) contains behavioural and 3T MR imaging data from 1206 healthy young adults who participated in the study between 2012 and 2015 [81].

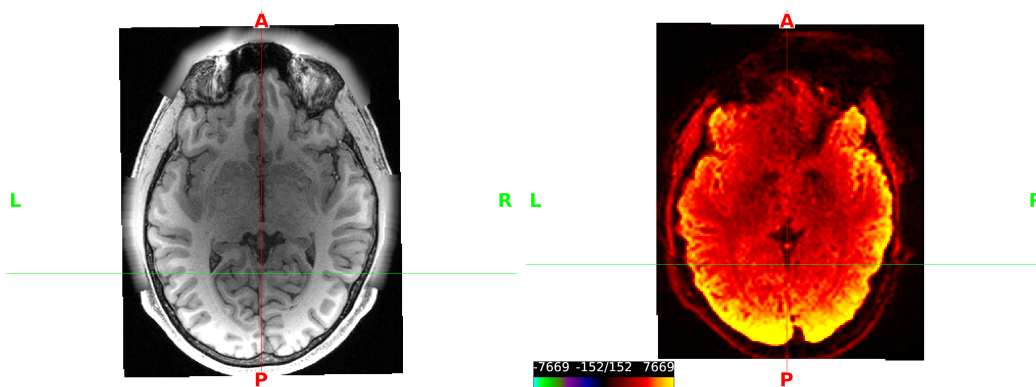
rfmri data were collected in four 15-minute runs across two sessions, with two runs each session. The subjects had their eyes open and had a relaxed fixation on a projected bright cross-hair on a dark background. The axial oblique varied within each session, between right-to-left (RL) in one run and left-to-right (LR) in the other run [82].

Table 3.1 shows the list of parameters from the dataset [82].

Table 3.1: Parameters used to collect resting state images [82].

Parameter	Value
Repetition time (TR)	720 ms
Echo time (TE)	33.10 ms
Slice thickness	2.0 mm
Slice number	72
Frames	1200
Voxel size	2.0 x 2.0 x 2.0 mm

Subject 100206's data was used for processing in this thesis. Preprocessed and unprocessed 3T data was downloaded from ConnectomeDB (Connectome Database). In the unprocessed data, the file *100206_3T_rfMRI_REST1_LR.nii.gz* was used as the functional file, shown in Figure 3.2. The file contains data from the resting state session one with a left-to-right (LR) direction. File *100206_3T_T1w_MPR1.nii.gz* is used as the structural file [82], shown in Figure 3.1. For processing data contains T1-weighted images and preprocessed data from the resting state session 1 with phase encoding in both left-right and right-left directions. During this project, left-right encoding was used.

**Figure 3.1:** Structural image, which is in the structural folder.**Figure 3.2:** Functional image that is in the functional folder.

The NIFTI volume file *rfMRI_REST1_LR.nii.gz* was used as an input to the self-made pipeline. *rfMRI_REST1_LR.nii.gz* is one of the outputs from HCP's Minimal Processing Pipelines, shown in Figure 3.3.

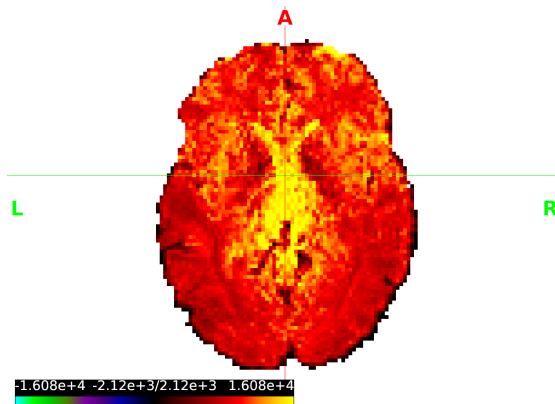


Figure 3.3: The figure shows the output from HCP's Minimal Processing Pipelines.

3.2 Minimal processing pipelines from Human Connectome Project

The Minimal Processing Pipelines have been applied to the unprocessed data by HCP. The processing pipelines consist of three sets of pipelines: structural pipelines, functional pipelines and a diffusion pipeline. After the structural pipelines have been completed, the functional pipelines or diffusion pipeline may run. Since the diffusion pipeline is not used during this project, it will not be further elaborated [82].

3.2.1 HCP Structural Pipelines

The HCP structural pipelines consist of three pipelines: PreFreeSurfer pipeline, FreeSurfer pipeline, and PostFreeSurfer pipeline [82]. The PreFreeSurfer pipeline has the main goals of producing undistorted native structural volume spaces for the subject, as well as aligning T1 and T2 weighted images, performing bias field correction and registering the native volume space to MNI space [82]. The bias field is an undesirable signal of low frequency that corrupts MRI images due to inhomogeneities in the magnetic fields of the MRI scanner [83].

The FreeSurfer and PostFreeSurfer pipeline's goals are to process and segment the volume data into cortical surfaces and create surface files. The data generated from these are not used in this thesis and are therefore not further elaborated [82].

3.2.2 HCP Functional Pipelines

The functional pipelines consist of the fMRIVolume pipeline and fMRISurface pipeline. For the intent of this thesis, the only relevant pipeline is the fMRIVolume pipeline. The fMRIVolume pipeline takes the fMRI data and removes spatial distortions, compensates

for subject motion by realigning the volume and registers the fMRI data to the structural data. The structural data is the output. In addition to this, the pipeline reduces the bias field, normalises the 4D image to a global mean, and finally masks the data with a brain mask. During the pipeline, there has been taken care to minimize smoothing effects from the interpolation, such that no unnecessary smoothing is being done. The output of this pipeline can be used in standard volume-based analyses according to the reference manual [82]. The output of this pipeline is the fMRI volume data referred to when HCP processed data is mentioned further in this thesis.

Chapter 4

Software

4.1 DPABI Matlab Toolbox

Volume-based data preprocessing of the HCP dataset was performed by using Data Processing Assistant for Resting-State fMRI (DPARSF [84]), which is based on Statistical Parametric Mapping (SPM12 [85]) and had been integrated into Data Processing and Analysis of Brain Imaging (DPABI [86]) [87].

The MATLAB programs DPABI and DPARSF are used to handle and analyze brain imaging data. DPABI is a software tool designed for preprocessing and analyzing fMRI data. DPARSF was created to offer a pipeline for processing and interpreting resting-state fMRI data. Many preprocessing procedures are necessary for resting-state and task-based fMRI data, including slice timing correction, motion correction, and spatial normalization, which are automated by DPARSF. It also includes several tools for artefact detection, data quality control, and functional connectivity. Although DPABI is a more complete software package that can be used for preprocessing and evaluating various brain imaging data [31].

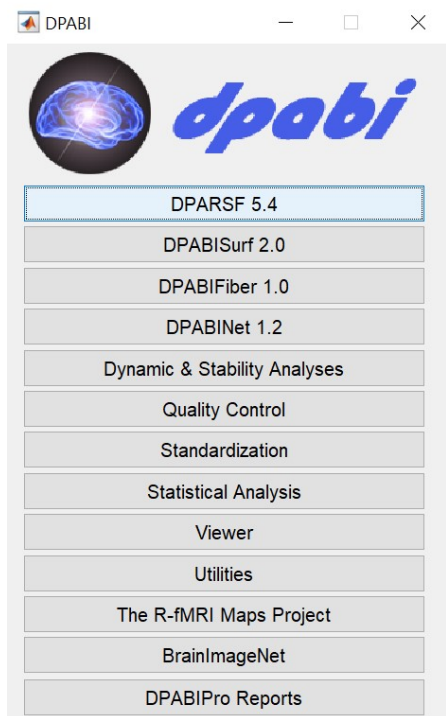


Figure 4.1: DPABI panel/
GUI

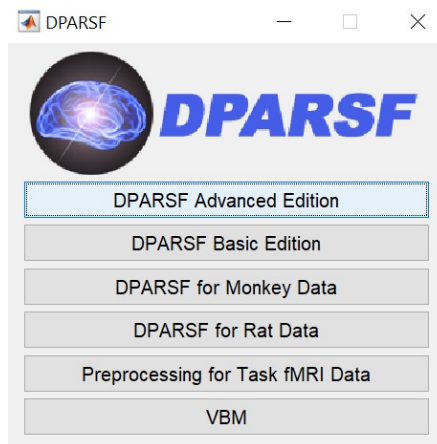


Figure 4.2: DPARSF panel/
GUI

There are a few procedures to be performed before using the DPABI toolbox. The first step is to install the SPM12 and DPABI toolboxes. The DPABI path is then included in the main environment using subfolders. Figure 4.1 will appear when *dpabi* is called in the MATLAB command window. Figure 4.2 will appear when the highlighted button in Figure 4.1 was pressed. To preprocess the fMRI data the highlighted button in Figure 4.2 was pressed.

The second step is data organization before using the DPABI toolbox. The dataset must be organized in a specific way to recognise the dataset. One must create a study folder, one with structural images and another with functional images. Within both structural and functional folders, there need to be subject folders. In each subject folder, all DICOM files will be placed. After organizing all data in this manner, the DPABI toolbox can be used [88].

4.2 Windows Subsystem for Linux

FreeSurfer and Connectome Workbench are programs that must run on a Linux-based operating system. Windows Subsystem for Linux (WSL) is a feature within Windows that allows the user to utilize a Linux command line and a Linux file system directly on Windows [89]. WSL was configured using Microsoft's guide for installing WSL [90]. The Linux distribution that was chosen was Ubuntu-20.04.

4.2.1 FreeSurfer

FreeSurfer is a software package that allows the user to analyse and visualise structural and functional neuroimaging data. The software package is a collection of tools for analysing neuroimaging data that includes a variety of algorithms for quantifying the functional and structural properties of the human brain. [91].

The installation of FreeSurfer was done based on a terminal session provided by FreeSurfer's website [92]. The terminal session gives instructions to download an older version of FreeSurfer. [FreeSurfer version 7.3.1](#) [93] is one of the newest version of FreeSurfer, and therefore this was chosen. The specific file to link within the terminal is "freesurfer_ubuntu20-7.3.1_amd64.deb". To use FreeSurfer, it is necessary to apply to FreeSurfer for a license and add a text file containing the license to the path in Linux.

4.2.2 Connectome Workbench

Connectome Workbench is a free and open source for visualisation and mapping neuroimaging data, particularly data generated by the Human Connectome Project. The software includes *wb_view*, a graphical user interface (GUI)-based visualisation platform and *wb_command*, which is a command-line program for performing a variety of algorithms tasks on, for instance, volume data. *wb_command* is necessary to run HCP data processing pipelines [94].

Workbench allows the user to explore data and activity both on the surface and within the volume of the brain. The software connects with ConnectomeDB to import data from a group of subjects and display that data in Workbench on a group brain atlas [94].

The ConnectomeDB is a data management platform containing all of the HCP's generated data. This includes image data, clinical evaluations, behavioural data, and other information [95]. The following command was written in the Ubuntu terminal "sudo apt-get install connectome-workbench" to Install Connectome Workbench.

Chapter 5

Method

5.1 Overview

DPABI Toolbox and Connectome Workbench were used to conduct volume-based functional connectivity analyses. DPABI Toolbox can be divided into preprocessing and resting state analysis, shown in Figure 5.1. The pink box represents preprocessing and shows all the steps involved. The green box shows the resting state analysis of the preprocessed data and produces a functional connectivity matrix.

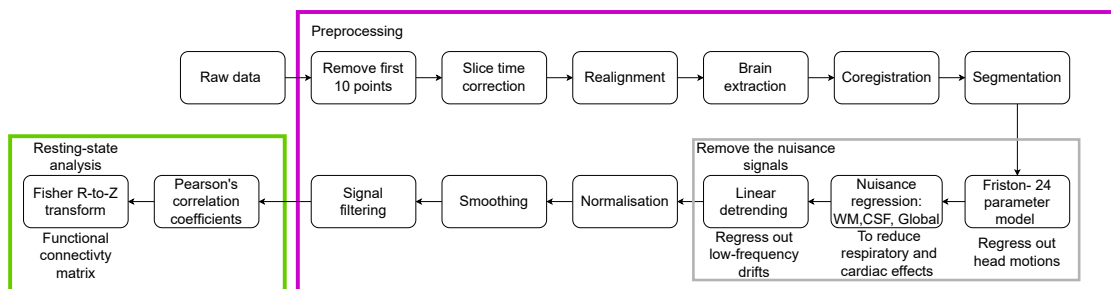


Figure 5.1: DPABI pipeline: HCP raw data are preprocessed (pink box), and resting-state analysis is performed to obtain a functional connectivity matrix (green box).

Connectome Workbench was used to create a pipeline for creating a resting state functional connectivity matrix. The pipeline uses CIFTI files, so the NIFTI inputs are converted to the CIFTI format. The resting state analysis can be performed on the raw data preprocessed by DPABI and the preprocessed data provided by HCP. A block diagram of the pipeline is shown in Figure 5.2.

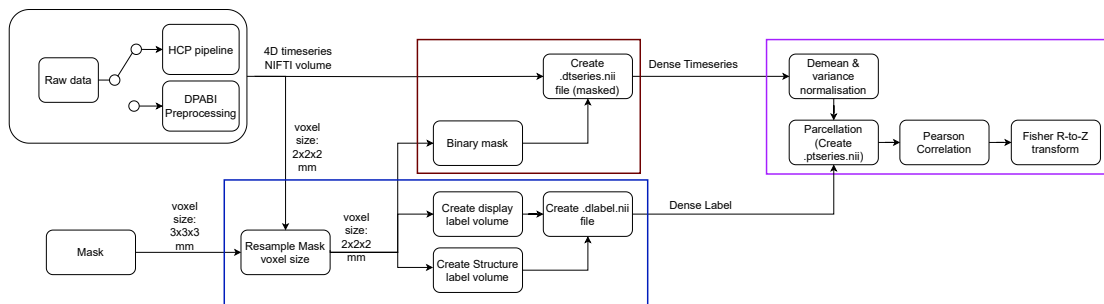


Figure 5.2: The block diagram has three main sections that coincide with the three main steps of the resting state analysis. The blue box (lower left) represents the steps involved in creating a dense label file, the red box (upper left) represents the steps involved in creating the dense time series and the purple box (upper right) represents the steps involved in creating the parcellated connectivity matrix.

5.2 DPARSFA

The DPARFA panel can be divided into two subpanels highlighted in Figure 5.3. The upper panel, marked in pink, consists of preprocessing parameters. The lower panel, marked in green, consists of options for resting state fMRI analysis. All the preprocessing options are based on functions from the SPM Toolbox [96].

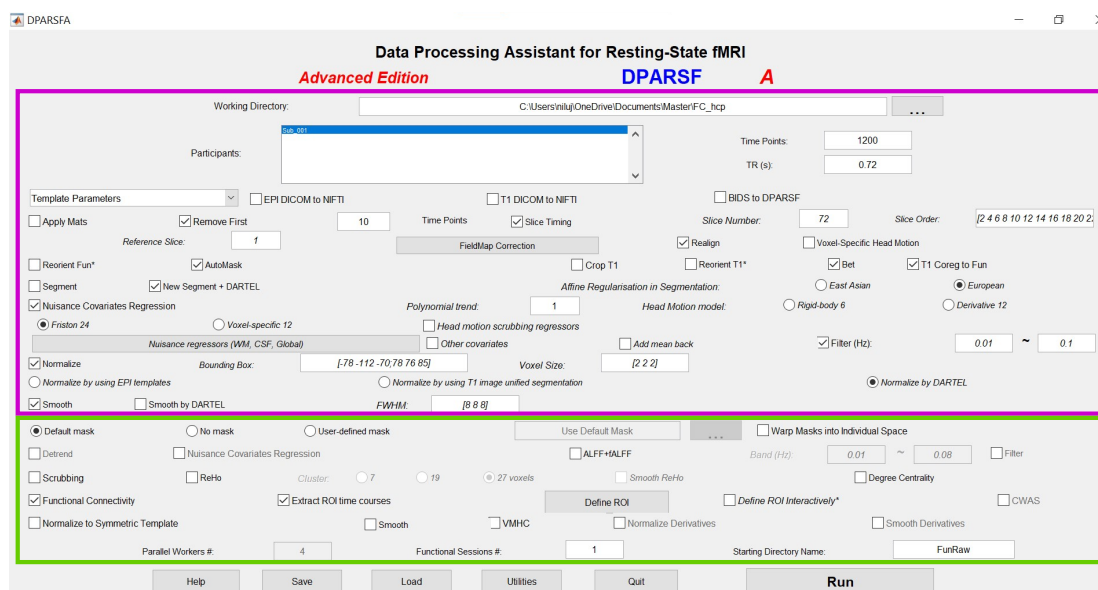


Figure 5.3: DPARSFA panel, where different parameters are defined. The upper pink box contains preprocessing parameters, and the lower green box contains options for resting state fMRI analysis. The colours of the boxes coincide with the boxes in the DPABI processing block diagram in Figure 5.1.

The working directory is the path to the directory containing the structural and functional folders. Figure 5.4 shows where to define the working directory and an overview of the subjects. As shown in the figure, this experiment only used data from one subject.

In the lower right corner of Figure 5.3, there is a starting directory; here, the functional folder must be defined. The functional folder is defined as "FunRaw" in the figure.

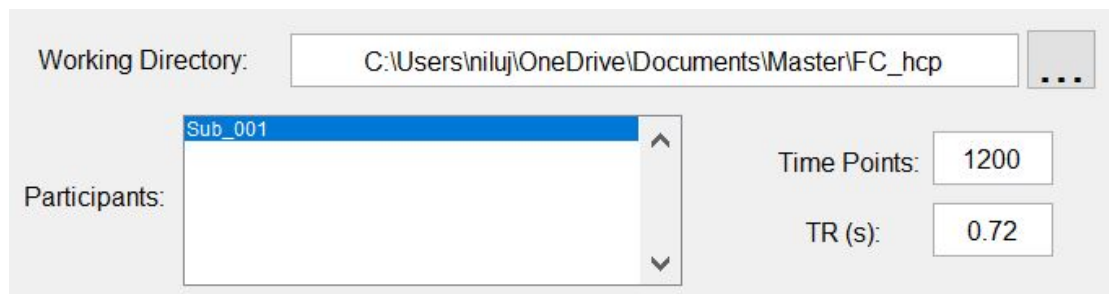


Figure 5.4: The figure shows where to define the working directory and where to put in time points and TR.

From Table 3.1, the time points and the repetition time (TR) are defined as 1200 and 0.72 s, as shown in Figure 5.4.

The preprocessing pipeline consisted of the following steps. The initial ten time points were discarded. Normally the first 5-10 time points are discarded or removed because the imaging will not reach a steady state, and the subject will not enter the rest state by that time [96].

Slice timing correction was applied by defining the following parameters: the slice number, slice order and reference slice. The slice number was set to 72 from Table 3.1, and the slice order was defined with all the even numbers first, followed by odd numbers up to 72. The slices were acquired on a 3T scanner (Siemens MAGNETOM ConnectomS syngo) with interleaved series mode and transversal direction from feet to head [82]. According to Table 2 in this paper [97], the slice order has to be defined as even to odd order in SPM since the dataset has an even number of slices. The reference slice was set to one and served as a template for the alignment process. This parameter corrects for differences in the acquisition times between slices in a volume of fMRI data. This helps reduce the effects of slice-dependent artefacts, as described in Section 2.5.1. Figure 5.5 shows the parameters used to define slice timing correction.

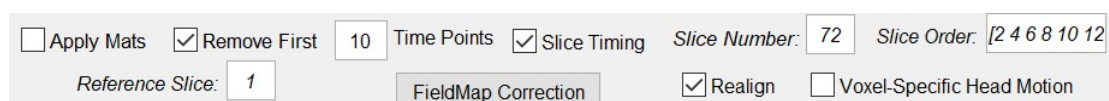


Figure 5.5: Slice timing parameters are defined, and realignment has been checked.

Realignment was also applied to correct the head motion during the fMRI scan, as shown in Figure 5.5. This ensures that the signal source in a particular voxel is always in the same physical location, as explained in Section 2.5.2.

The AutoMask box was checked to automatically extract the brain from the rest of the skull for each realigned image. This will remove non-brain tissues, such as the skull, scalp, and meninges, but also removes noise. Bet was applied if the AutoMask failed to extract the brain accurately because of artefacts or image noise [96]. Bet was applied for better coregistration as described in Section 2.5.3. Figure 5.6 shows that both AutoMask and Bet have been applied to the fMRI data.



Figure 5.6: Automask, brain stripping algorithm BET, and T1 coregister functional image have been checked.

Each T1 anatomical image was coregistered with a functional image. The goal is to accurately map functional data onto the underlying brain anatomy so that the structural and functional images are in the same space, explained in Section 2.5.4).

The "New Segment + DARTEL" method segments T1 weighted structural images and applies the DARTEL algorithm to normalise the results to a standard template. The "New Segment" function segments T1 weighted images into grey matter, white matter, and CSF. This function creates tissue probability maps that show the likelihood that each voxel is a part of the CSF, white matter, or grey matter [98]. The "DARTEL" method prepares T1 weighted images that normalise each subject's data to a standard brain template. These two methods combine segmentation and normalization into a single workflow, which provides a common reference area for comparing functional connectivity patterns among subjects, explained in Section 2.5.8. Figure 5.7 shows that "New Segment + DARTEL" was performed on the data.



Figure 5.7: Segmentation, nuisance regression and filtering have been selected.

The affine regularisation in segmentation was applied for European brain. Nuisance covariate regression was applied, where the polynomial trend was set to 1 (linear detrend), the head motion model was set to Friston 24, and nuisance regressors were WM, CSF, and global, as shown in Figure 5.7. This polynomial trend has the potential to reduce the effects of low-frequency drifts. The Friston 24 model was used to regress the head motions. White matter, CSF, and global signals were estimated to remove covariance and were used as nuisance regressors. This was done to reduce noise and minimize the

error. The bandpass filter was set to 0.01-0.1 Hz to remove low- and high-frequency physiological noise.

Spatial normalisation was performed by defining the bounding box, voxel size and "Normalize by DARTEL", as shown in Figure 5.8. The bounding box refers to the region of interest (ROI) used for skull stripping, and the default values were used. The voxel size was set to 2 mm, as shown in Table 3.1. "Normalize by DARTEL" was applied since the "New Segment + DARTEL" method was used. Structural differences and similarities between groups or individuals can be studied more precisely by normalising structural MRI images to a standard template using DARTEL [98].

Normalize Bounding Box: [-78 -112 -70; 78 76] Voxel Size: [2 2 2]
 Normalize by using EPI templates Normalize by using T1 image unified segmentation Normalize by DARTEL
 Smooth Smooth by DARTEL FWHM: [8 8 8]

Figure 5.8: Normalization and smooth have been applied to the data.

Spatial smoothing was applied by setting the FWHM to 8 mm. This is because the literature's most commonly used smoothing level is 8 mm FWHM, which also is the default value in SPM [99]. The default mask is called a binary mask image, which removes non-brain tissues [98].

Since the goal was to perform functional connectivity analysis, the functional connectivity was selected, as shown in Figure 5.9. The extracted ROI time courses option was selected to enable DPABI to extract all the ROI time courses and use this to calculate other similarity assessments.

Functional Connectivity Extract ROI time courses Define ROI Define ROI Interactively* CWAS
 Normalize to Symmetric Template Smooth VMHC Normalize Derivatives Smooth Derivatives
 Parallel Workers #: 4 Functional Sessions #: 1 Starting Directory Name: FunRaw

Figure 5.9: Functional connectivity has been chosen for resting state analysis.

Once functional connectivity is selected, the "Define ROI" button is activated. The "Define ROI" button allows the user to choose standardised atlases. The chosen atlas was "/Power_Neuron_264ROIs_Radius5_Mask", as shown in Figure 5.10.

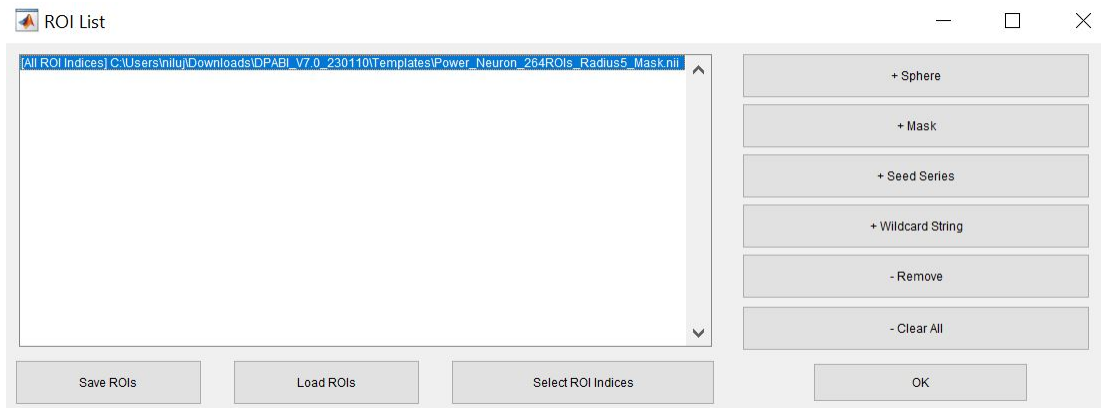


Figure 5.10: Defining the ROI as the Power el at. atlas.

Once everything has been defined, the preprocessing and resting state analysis can be initiated. During the preprocessing of fMRI resting-state imaging, a warning message may appear, indicating that the system is unable to detect the coregistered T1 images automatically. In such cases, a prompt will ask if the original T1 weighted imaging should be used as the imaging process. To apply coregistration to the original T1 image, this prompt should be accepted.

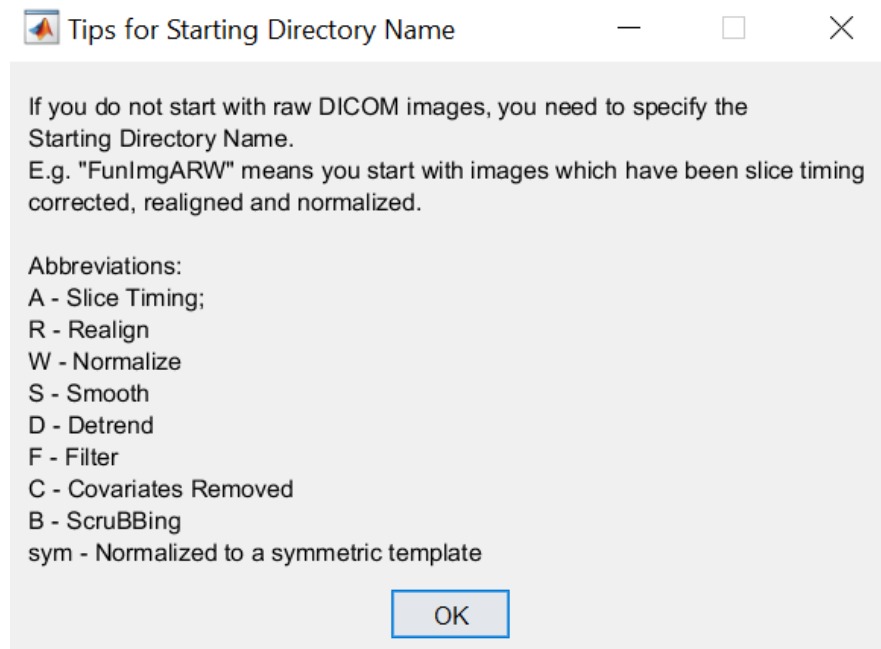


Figure 5.11: Abbreviations of folders produced by DPABI.

When all the processing is completed, there will be a message in the command window that says that the processing is done. The Working Directory will contain various folders corresponding to different preprocessing steps. Figure 5.11 FunImgARC indicates that folders have images that have been slice timing, realigned, and covariates removed. The

most significant folder is the result folder, containing the correlation coefficient map for subsequent analysis and visualisation.

5.3 Pipeline when using Connectome Workbench to make functional connectivity matrix

When using Connectome Workbench to make a functional connectivity matrix the created pipeline was based on a pipeline [100]. The pipeline makes a dense data series file and a dense label file and creates a functional connectivity matrix from these. Tjihuis et. al's pipeline uses CIFTI dense data series (.dtseries) and dense label (.dlabel) files as inputs, while the files being inserted into the pipeline created in this project are NIFTI files. The first file is a 3D NIFTI mask, and the second file is a 4D NIFTI volume file containing the time series. It is, therefore, necessary to convert the NIFTI files into their respective CIFTI formats before being used in the final pipeline. The resting state analysis pipeline was applied to both the raw data preprocessed by DPABI and the raw data preprocessed by HCP. Only the preprocessed raw data from HCP will be displayed throughout the steps of the pipeline.

5.3.1 Making a dense label file

The first step in the developed pipeline is to create a dense label file. Dense label files have .dlabel.nii as their extension and store named label maps across vertices and voxels. Each label map has a separate label table defined within the CIFTI XML. A row is a single label value from each named label map for one vertex or voxel [77].

The pipeline that creates this dense label file centres around the utilization of the *-cifti-create-label* function from the Workbench Command, which makes the dense label file from the NIFTI file `Power_Neuron_264ROIs_Radius5_Mask`. The online documentation [101] provides detailed information about this function. There are several optional input variations in the documentation, but the most relevant for this project is the option named *-volume*. This option requires a label volume and a structure label volume. The label volume is a volume containing the labels that will be displayed. The structure volume contains a set of labels from the list of CIFTI brain structures found in [77]. Structure names that are not from the full list are ignored, and the voxels in the dense label file from these areas are not included.

The NIFTI time series file from HCP has been transformed from its native space to MNI152, and the `Power_Neuron_264ROIs_Radius5_Mask` is also in MNI152 space. The mask has a voxel size of 3 mm, while the time series has a voxel size of 2 mm. Therefore an affine transformation is applied to the `Power_Neuron_264ROIs_Radius5_Mask` to

achieve a voxel size of 2 mm. Figure 5.12 shows the original mask, and Figure 5.13 shows the mask after the affine transformation. It can be observed that the highlighted pixel in both of the figures has the same index value of 232. The voxel coordinate in XYZ measured in mm are the same, but the voxel indices differ. In Figure 5.12, the voxel indices are (40, 38, 24), while in Figure 5.13, the voxel coordinates are (60, 57, 36). This change in voxel indices happens because the voxel size change from 3 mm to 2 mm. The change in voxel indices is 1.5 times larger in Figure 5.13 than in 5.12. The scaling also changed the shape of some of the regions slightly.

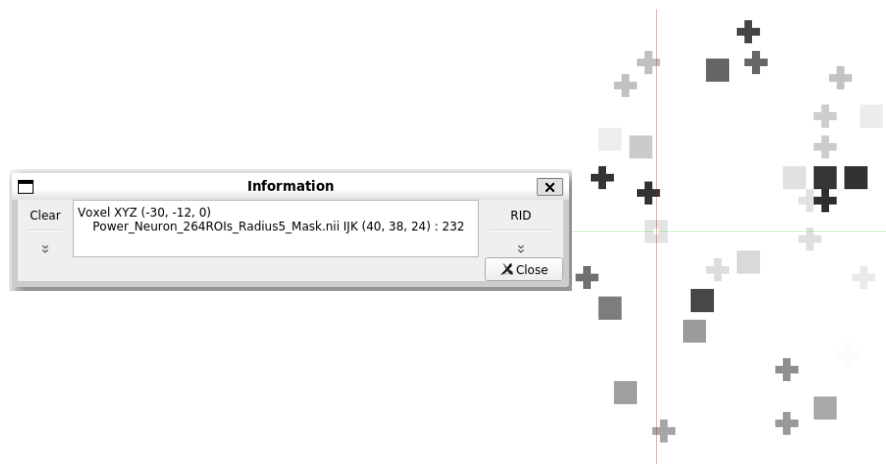


Figure 5.12: This figure shows a slice from the original Power et al. mask. The crosshair highlights the x-, y- and z-coordinates (-30, -12, 0) in mm, the voxel indexes (40, 38, 24) as well as the voxel value of 232. The mask has a voxel size of 3 mm and is in MNI space.

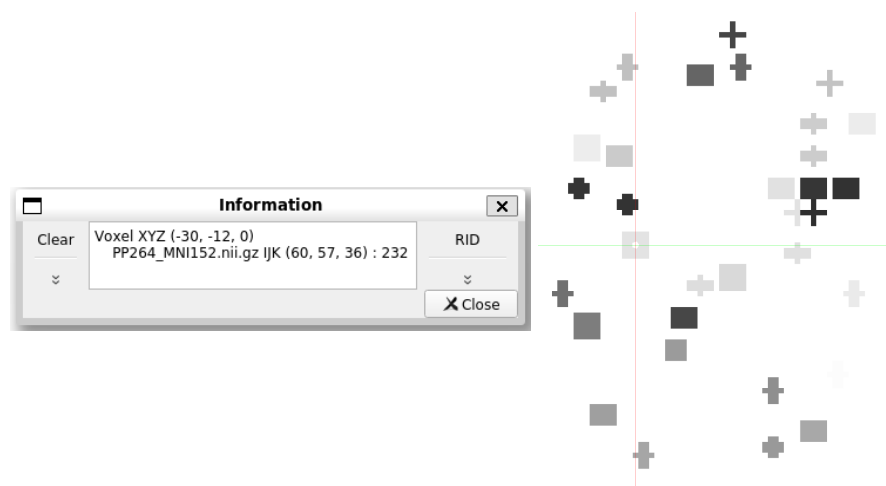


Figure 5.13: This figure shows a slice of the Power et al. atlas after the affine transformation has been applied to it. The crosshair highlights the x-, y- and z-coordinates (-30, -12, 0) in mm, the voxel indexes (60, 57, 36) as well as the voxel value of 232.

The Workbench Command function *-volume-label-import* was used to make the label volumes. The function takes a volume file and a text file as inputs and produces a label volume. The text file contains the label name, the index the label is associated with and colour specifications. The colour specifications have the format R G B α , where R, G, and B are the colour channels red, green and blue. α denotes the opacity of the colour. The format of the text file is shown in Figure 5.14.

```

<Label_name1>
idx1 R1 G1 B1  $\alpha$ 1
<Label_name2>
idx2 R2 G2 B2  $\alpha$ 2
...
<Label_nameN>
idxN RN GN BN  $\alpha$ N

```

Figure 5.14: Label table format

The created label volumes are the display and structure label volumes to be inserted into *-cifti-create-label*. The display label volume is created using the scaled Power et al. mask as the volume input to *-volume-label-import*. The label table uses the indexes from the scaled mask as label names and indexes. The colours are set to match the functional networks shown in Table 2.1, and the opacity (α) is set to the highest setting of 255. Figure 5.15 shows one slice of the display label volume.

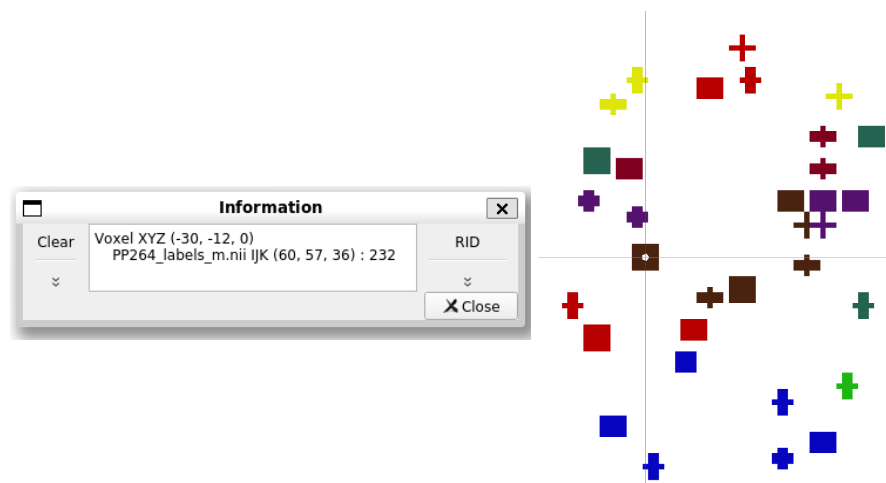


Figure 5.15: This figure shows a slice of the display label volume. The highlighted voxel displays "232" which is the label corresponding to the value 232 in the Power et al. atlas.

To make the structure label volume, the brain structure CIFTI_STRUCTURE_OTHER was chosen. This avoids the need for manual labelling of the structures, as it is not required for the label structure volume to function as intended. The scaled Power et al. mask needs to become a binary mask containing the same voxels as the mask. This is achieved by applying a comparison operator $x > 0$ for all voxels, where x is an individual voxel. Every voxel that satisfies this inequality is set to 1. The binary mask is then used to create the structure label volume by combining the binary mask with a label table. The label name is set to "OTHER" and the index is set to 1. The colour choice is arbitrary and was set to blue. Figure 5.16 shows one slice of the structure label volume. The value displayed in the structure label volume is the label "OTHER".

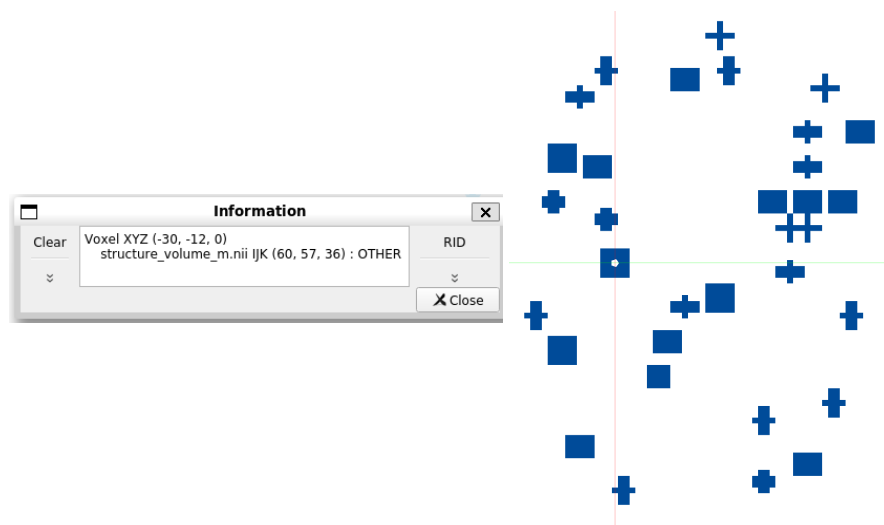


Figure 5.16: This figure shows one slice of the structure label volume. The highlighted voxel now has a value of OTHER.

The display label volume file and the structure label volume are then combined using *-cifti-create-dense-label*. One slice of the finished dense label file is shown in Figure 5.17. In the information box, it can be observed that the file name contains *.dlabel*, and it is specified that the labels are CIFTI labels.

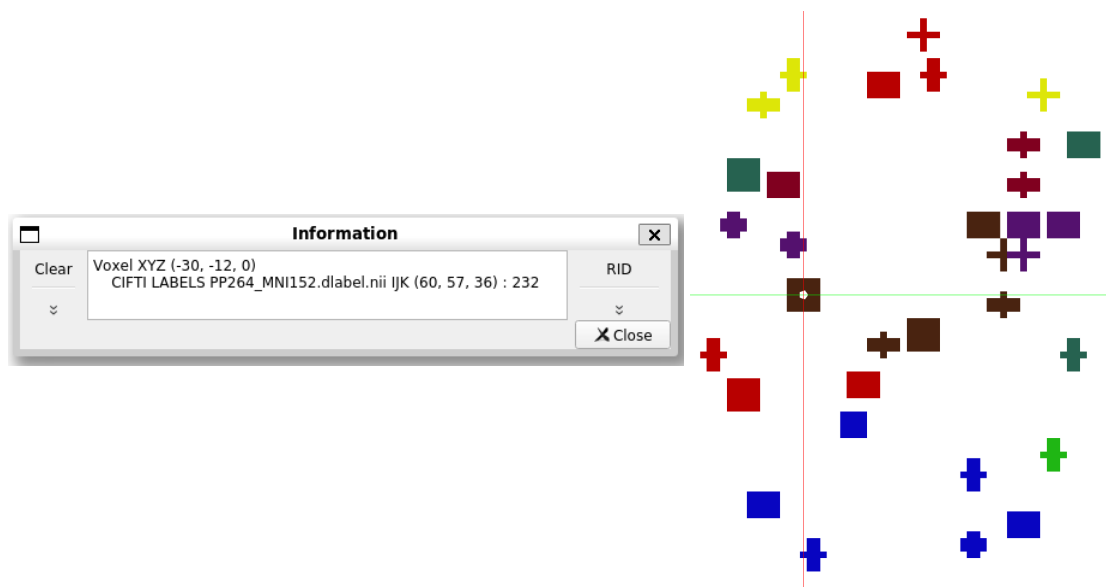


Figure 5.17: Dense label file created in the developed pipeline. The colours of the label file match up with the nodes in the Power et al. atlas. The number shown in the information box is a CIFTI label with the label '232', which matches the index of the ROI from the atlas.

5.3.2 Making a dense time series file

The dense data series has the file extension `.dtseries.nii` and represents data points in a series for every voxel and vertex in the mapping. The dense data series has a series mapping along the rows, and along the columns, it has brain models mapping. The series mapping contains attributes such as the number of points, start, step and unit. Most of the time, the series is a time series, but it can also represent other data types, such as measurements of frequency (Hz), distance (m) or angles (radians) [77].

Creating a dense time series file in this pipeline centres around utilising the `-cifti-create-dense-timeseries` from workbench command [101]. Function `-cifti-create-dense-timeseries` has several input options related to the CIFTI file format. The inputs used in this project are `-volume`, `-timestart`, `-timestep` and `-unit`. The `-volume` option has two inputs: volume data and structure label volume. The volume data is the 4D NIFTI volume time series that will be transformed into the CIFTI dense data series format. The structure label volume contains label data, acts like a mask that removes voxels that will not be examined, and connects the data to brain structures in the CIFTI format.

The scaled Power et al. mask is used as a foundation to create the structure label volume. The only brain structure that will be included in this project is the `CIFTI_STRUCTURE_OTHER` from Table 2.3, for the same reasons as described in Section 5.3.1 about creating a dense label. The scaled mask is then thresholded and

transformed into a binary mask by applying the comparison operator $x > 0$ for all voxels, where x is an individual voxel. The result of the thresholding is shown in Figure 5.18.

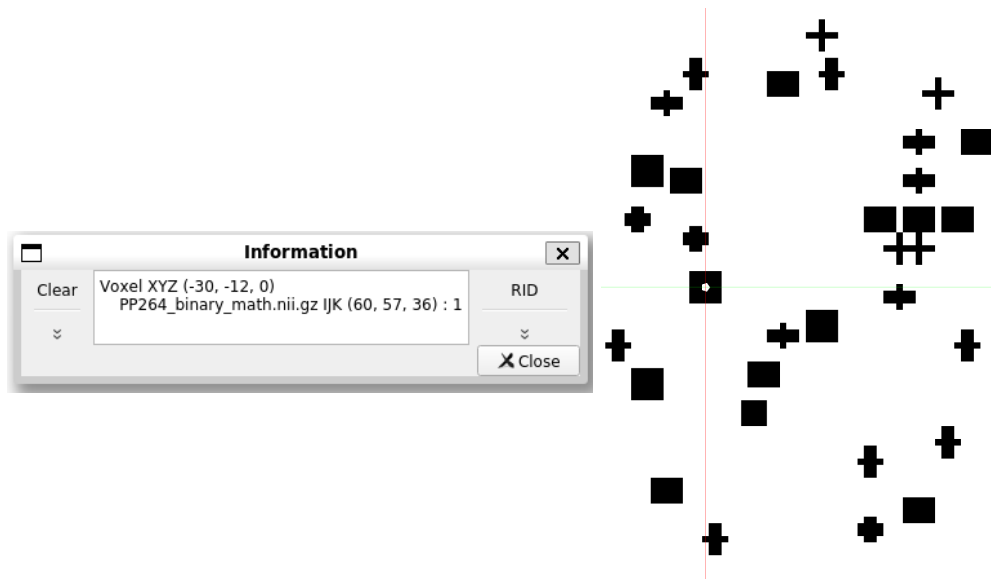


Figure 5.18: The figure shows the binary mask used to create the label structure volume. The highlighted voxel is the same as in Section 5.3.1.

The binary mask is then used to create the label structure volume to be inputted to *-cifti-create-dense-timeseries*. *-volume-label-import* is used as described in Section 5.3.1, when describing how to create a label structure volume. Figure 5.14 is used as a template, and the label name is "OTHER". The index is set to 1, and the chosen colour is set to blue. The opacity is set to 255. Figure 5.19 shows the label structure volume.

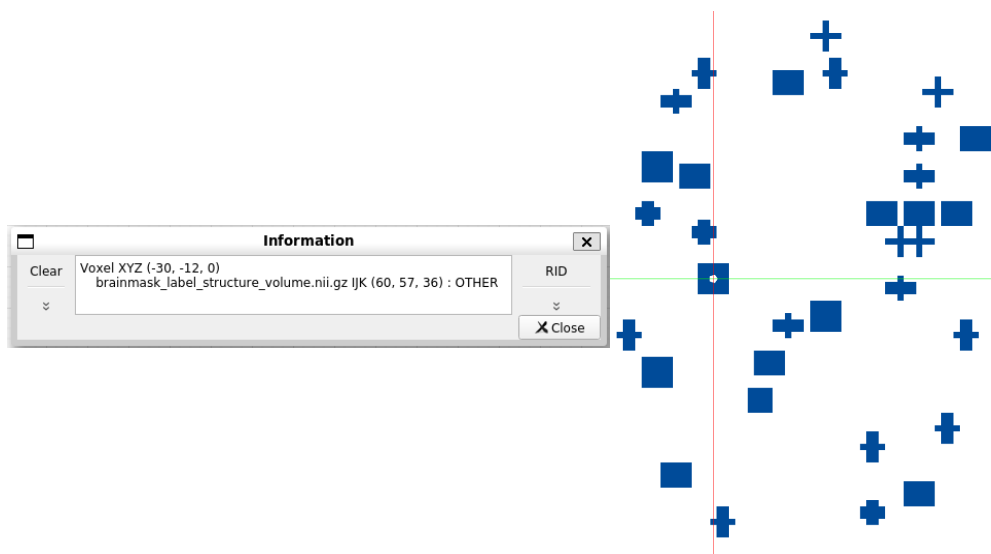


Figure 5.19: The figure shows the structure label volume used to create the dense time series. The label "OTHER" is displayed as the value of the highlighted voxel.

When the label structure volume has been created the dense label file can be constructed using *-cifti-create-dense-timeseries*. The 4D NIFTI time series is set as the data volume, and the created label structure volume is set as the structure label volume option. The starting time is set to 0, the time step is set to 0.72, following Table 3.1, and the unit is set to seconds. The resulting dense time series file is shown in Figure 5.20.



Figure 5.20: The figure shows the dense time series file created in the developed pipeline. The highlighted voxel has a data series value of 11058.3 at time point 0 s.

5.3.3 Making of parcellated functional connectivity matrix

The final step of creating a parcellated connectivity matrix is based on the pipeline created by Tijhuis et al. [100]. The pipeline creates a parcellated connectivity file from a dense label and a dense data series. The dense data series is parcellated using the dense label to achieve this.

A parcellated data series has the extension *.ptseries.nii* and represents data points in a series for areas of the brain. The parcellated data series has a series mapping along the rows and a parcel mapping along the columns. The parcel element associates a name and voxel and/or vertice data to an index [77].

Parcellated connectivity files have the extension *.pconn.nii* and represent connectivity between parcels or areas of the brain. Each row represents the connectivity from one parcel from the column to all the parcels within that row. Using "from" and "to" does not imply directly that the data is always directed but acts as a convention for directed data. The parcellated connectivity files can contain a single mapping along both axes, such as in this project, or it can contain different groups of parcels, creating an asymmetric matrix [77].

The first step in this preprocessing step is to demean, and variance normalise the dense time series data. According to Tjihuis et al. in the manual of their GitHub repository [100], the demeaning and variance normalisation is done to standardise the data for concatenation. A slice of the demeaned and variance normalised dense time series is shown in Figure 5.21.



Figure 5.21: The figure shows a slice of the demeaned and variance normalised dense time series file at time point 0 s.

The next step is to parcellate the dense time series. This is done by applying *-cifti-parcellate* from Connectome Workbench to the dense time series with the created dense label as a parcellation template. When parcellating, it is necessary to specify which mapping to parcellate. For this data, the parcellation will be applied to the columns of the dense time series, since it contains the brain model mapping. Then the specified voxels can be associated with a label/parcel. The choice of parcellation method was the mean of the voxels within each parcel, which is the standard choice for the command. A slice of the parcellated time series is shown in Figure 5.22.



Figure 5.22: This figure shows a slice of the parcellated time series at timepoint 0 s. The information box shows which parcel the specific voxel belongs to and the mean value of all the voxels within that specific parcel.

The final step of the pipeline is to create the parcellated connectivity matrix and store the data. This is done using the *-cifti-correlation* from Connectome Workbench. This function uses the parcellated time series as input, calculates the correlation between all the parcels and organises the correlation values in a matrix on the parcellated connectivity format `.pconn.nii`. The function is called twice; one time for calculating the Pearson correlation and one time to calculate the Pearson correlation and apply the Fisher R-to-Z transform to the correlation data. The data within parcellated connectivity files are also stored as text files for easy access in Python.

Chapter 6

Results and Discussion

Functional connectivity matrices for all the experiments were achieved by using the Pearson correlation for each pair of regions. Then each correlation coefficient underwent a Fisher z-transformation to improve the spatial normality of the correlation value distribution. When calculating the Structural similarity using SSIM it is required to provide the dynamic range of the input images. The floating points of the matrices are therefore converted into 64-bit unsigned integers, which results in $L = 2^{64} - 1$.

6.1 DPABI

A 264×264 functional connectivity matrix produced from raw data from HCP is shown in Figure 6.1. Preprocessing and resting-state analyses were performed using DPABI. Each node is defined according to the Power et al. atlas on the x-axis, marked by different coloured boxes. The colour bar indicates the range of the correlation between each ROI pair, which ranges from just below -0.2 to slightly above 1.6.

The matrix in Figure 6.1 can be divided into diagonal and off-diagonal elements. The diagonal elements can be ignored since they show the correlation between the nodes themselves. The diagonal elements have a correlation value of ∞ due to the Fisher R-to-Z transform and contain no information of interest. The off-diagonal elements show the connectivity between pairs of different nodes, which can be divided into the upper and lower triangle. It can be observed that the matrix is symmetric about the main diagonal, so the upper and lower triangle are identical. From Equation 2.2 describing the Pearson correlation, it can be observed that in the comparison between X_i and Y_i the same operations are done to the variables. This means that the order of operation does not matter, resulting in a symmetrical matrix about the main diagonal. This symmetry can be observed in Figure 6.1.

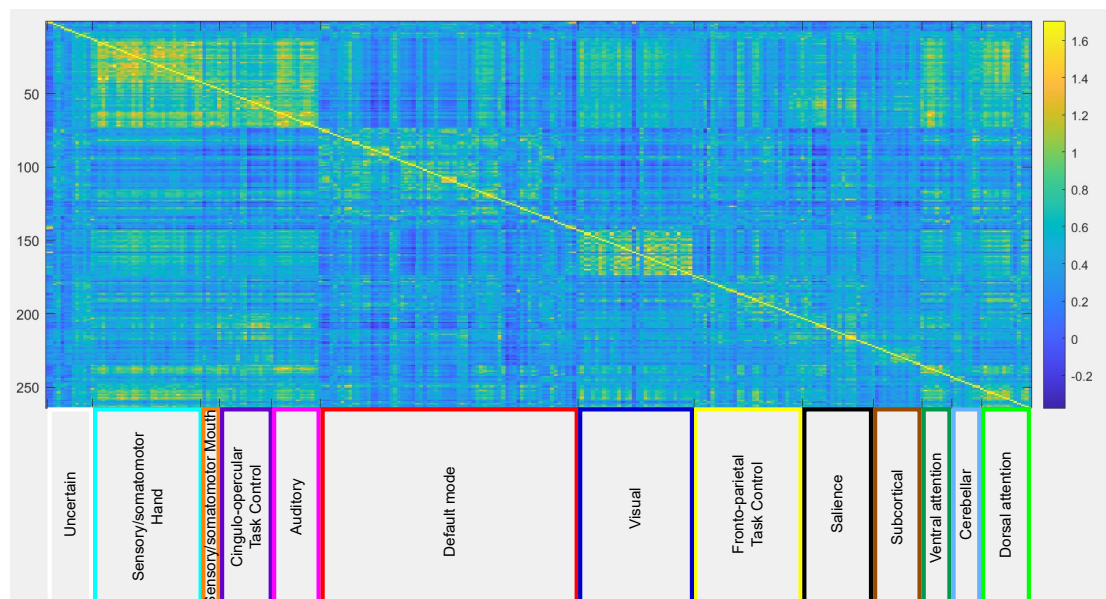


Figure 6.1: A 264 x 264 matrix produced by DPABI where each node is labelled according to Table 2.1 describing the colours of the different functional networks.

Figure 6.1 shows a block-like structure of higher correlation which can be observed along the diagonal of the matrix. These allude to higher functional connectivity for nodes that belong to the same system for this subject.

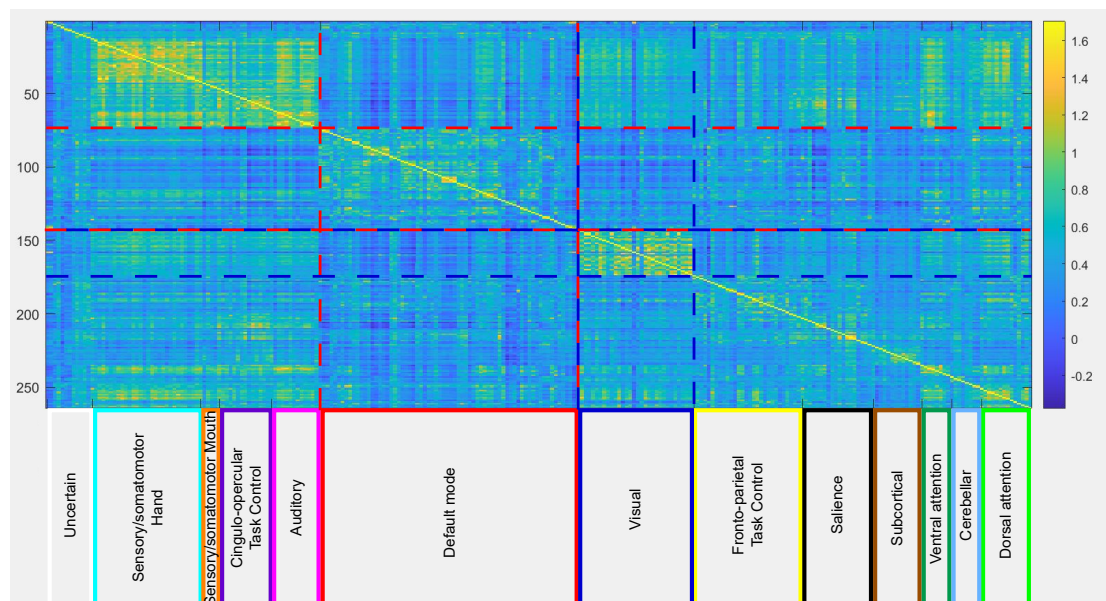


Figure 6.2: The default mode network is marked with a red dashed line, and The visual network is marked with a blue dashed line.

The default mode network seems to correlate mostly with itself and seems to have a lower correlation with other networks, as shown in Figure 6.2. This is highlighted by red

dashed lines, where the areas within the rows and columns related to the default mode are bluer than the rows and columns related to the visual networks.

The visual network is marked with a blue dashed line and has some correlation with other networks such as the sensory/somatomotor hand. This means that the fluctuation from the visual network is similar to that from the sensory/somatomotor hand. The visual network has a high correlation, which makes sense because the subjects had their eyes open during the data acquisition.

6.2 Comparison between DPABI toolbox and Connectome workbench

Figure 6.3 shows the functional connectivity matrices of data preprocessed in DPABI Toolbox. Resting state analysis was performed in DPABI Toolbox, where the resulting matrix is shown in Figure 6.3a. Figure 6.3b shows the matrix where the resting state analysis was performed in Connectome Workbench.

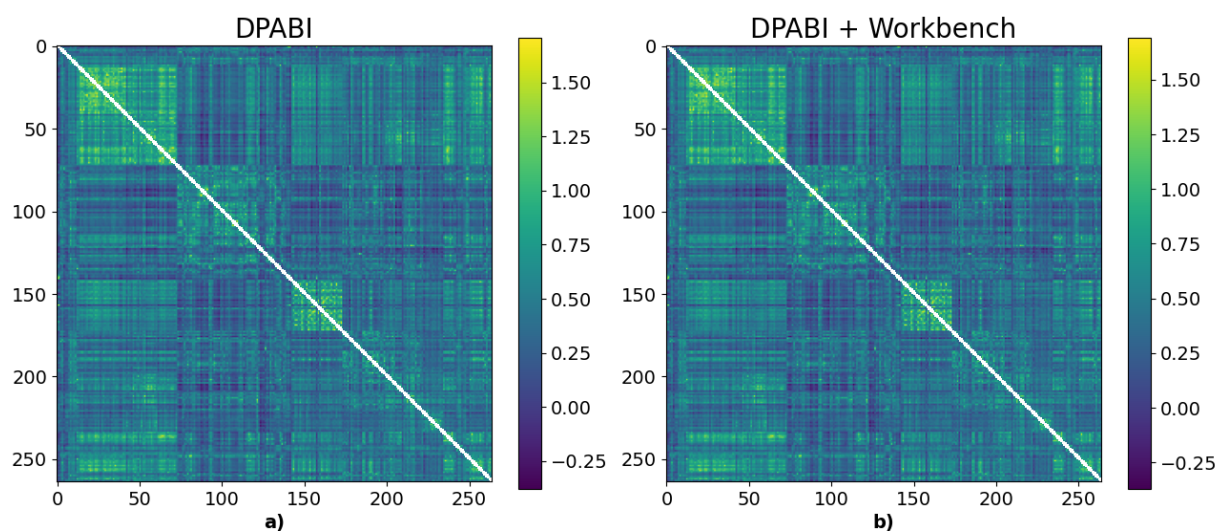


Figure 6.3: a) Raw data processed by DPABI, FC-matrix from DPABI. b) Data preprocessed by HCP pipeline, FC matrix created by connectome workbench through Linux command line.

By visual inspection, there seem to be no observable differences between the two matrices. The similarity metrics were performed to see any possible differences on both matrices and the results are shown in Table 6.1.

From the table, it can be observed that there are some small differences as indicated by the SSIM value of 0.998. MSE and UQI achieved a result of 0.000 and 1.000. The values are rounded to 3 decimal points, so there are most likely some very small differences that

are present in both MSE and UQI. These differences must be present at the 4th decimal point or later. This is the case since every pixel/element must have the same value to achieve the best SSIM score of 1 as described in Section 2.7 about metrics. The result shows that the self-made resting state analysis pipeline has comparable results to the DPABI pipeline.

Table 6.1: The table shows the similarity between the matrices in Figure 6.3

	DPABI \times DPABI+Workbench
SSIM	0.998
MSE	0.000
UQI	1.000

6.3 Comparison between the HCP preprocessed data and our preprocessed data

Figure 6.4 shows two functional connectivity matrices. The Matrix from Figure 6.4a is produced using HCP's raw data, and DPABI for both preprocessing and calculation of the functional connectivity. The matrix from Figure 6.4b is produced by using preprocessed HCP data which has been fed through the self-made pipeline based on Connectome Workbench. The colour maps are the same, and both matrix from Figure 6.4 a and b has a range of approximately -0.25 to 1.5.

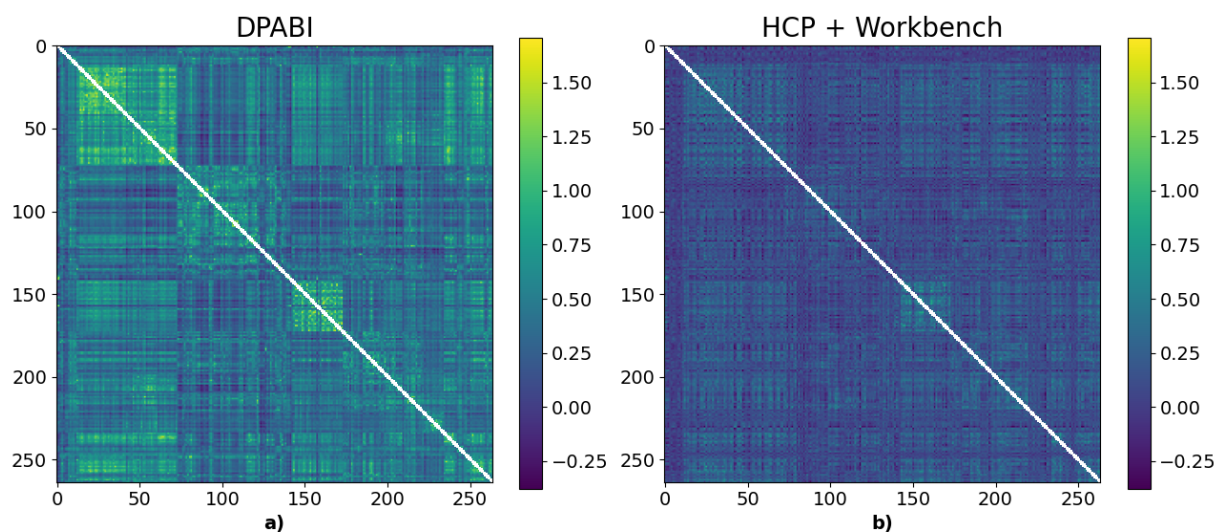


Figure 6.4: a) Raw data processed by DPABI FC-matrix created by DPABI. b) Raw data processed by HCP preprocessing pipeline, FC-matrix created with Connectome Workbench.

From Figure 6.4, it can be observed that the two matrices have similar structures, but different intensities. The diagonal from DPABI is ∞ and therefore the diagonal values have been removed from the matrix and appear to be white. The maximum value of matrix b was 7.254, which is significantly larger than the off-diagonal values of matrix b. The diagonal elements are not of interest, since they represent functional connectivity with themselves, as described in Chapter 2.3. By removing the diagonal values, the contrast from the off-diagonal values was increased when displaying the matrices. It can be observed that the default mode has lower connectivity to the other networks in both of the matrices. In Figure 6.4a the connectivity within the default network is higher compared to Figure 6.4b where it is barely visible.

6.4 Metrics

Table 6.2 lists the overall results of the experiments performed in this study. The rows show the different metrics used to evaluate the similarity between the matrices and the columns show a comparison of different matrices. The first column shows the metric values of comparing the functional connectivity of the preprocessed raw data and the resting state analysis on DPABI. The column represents an ideal comparison.

The second column in Table 6.2 shows the similarity metrics when comparing the matrices from Figure 6.3a and b. These values are almost the same as the ideal values as described in Section 6.2.

Table 6.2: The table shows an overview of the measured metrics.

	DPABI \times DPABI	DPABI \times DPABI+Workbench	DPABI \times HCP+Workbench
SSIM	1.000	0.998	0.218
MSE	0.000	0.000	0.107
UQI	1.000	1.000	0.348

The last column in Table 6.2 shows the similarity metrics when comparing the matrices from Figure 6.4a and b. The SSIM and UQI index quantify structural differences of the matrices shown in Figure 6.4.

When comparing the last column with the ideal result (first column), the difference in the SSIM index is 0.782. The difference between the UQI index and the ideal UQI index is 0.652. The MSE has a value of 0.107. This indicates that, on average, each element in the matrices have a squared difference of 0.107. Calculating the square root of MSE shows that, on average, the difference between the elements in the matrices is 0.327.

6.5 Discussion

The original problem description was to compare volume-based analysis with surface-based analysis. This is the reason for installing FreeSurfer in Linux. This problem description had to be abandoned mid-way due to a discovery that when the Linux-based pipeline had been developed, it was a volume-based approach. Since it had taken months to develop the volume-based pipeline (Linux), it was not feasible to develop a new surface-based pipeline in the given time frame.

Connectome Workbench

The basis for the self-made pipeline was the pipeline developed by Tjihuis et al. [100], as described in Chapter 5. The inputs to the pipeline are a dense label file and a dense data series. During the development, understanding how to make these files would prove difficult when new to the field of neuroimaging. Finding relevant coding examples for creating the CIFTI formats proved difficult. Most search results showed how to use the CIFTI formats, not their creation. The documentation of Connectome Workbench [101] contains 206 commands that operate on different types of mappings, such as volumes, surfaces, CIFTI files and other utilities. In addition to Connectome Workbench and Freesurfer were downloaded to add to the arsenal of available tools.

Due to many commands and the scarcity of relevant coding examples, Chat-GPT was used to discover potentially relevant commands. Figure 6.5 shows a snapshot of a conversation with Chat-GPT about creating dense label files. Chat-GPT outputs a shell script containing the Connectome Workbench command *-volume-label-import*. Chat-GPT suggests that the output of *-volume-label-import* is a dense label file, but the output of this command is a label volume, as described in Chapter 5.3.1. The suggested label table is also in the wrong format. Therefore, Chat-GPT's information is wrong, and the result will not be directly implementable. However, the result highlighted the label import command used in the final pipeline, showing the usefulness of Chat-GPT. By using Chat-GPT, narrowed the search process to a couple of commands that could be further inspected and evaluated for the task. This approach was more efficient than reading about all the commands.

I have a NIFTI volume atlas file with indexes showing nodes of interest and I want to make it into a dense label dlabel file. create a linux shell script to do this, using either wb_command, fsl or freesurfer

Certainly! Here's a Linux shell script that uses the `wb_command` tool from Connectome Workbench to convert a NIFTI volume atlas file into a dense label dlabel file:

```
bash Copy code  
  
#!/bin/bash  
  
# Path to the input NIFTI volume atlas file  
input_nifti="path/to/input/atlas.nii.gz"  
  
# Path to the output dlabel file  
output_dlabel="path/to/output/atlas.dlabel.nii.gz"  
  
# Path to the label table text file (replace with your own label definitions)  
label_table="path/to/label_table.txt"  
  
# Convert NIFTI to CIFTI  
wb_command -volume-label-import "$input_nifti" "$label_table" "$output_dlabel"  
  
echo "Conversion complete!"
```

Make sure to replace the `input_nifti`, `output_dlabel`, and `label_table` variables with the appropriate paths for your files. The `label_table` file should contain label definitions in the following format:

```
python Copy code  
  
1 Label1  
2 Label2  
3 Label3  
...  
...
```

Figure 6.5: This is a snapshot of a conversation with OpenAI's natural language model Chat-GPT 3.5. The blue (upper) box shows the input to Chat-GPT, while the red (lower) box shows the model output.

The main challenge during the pipeline creation was understanding how to combine the dense label and the dense time series file when parcellating. The first naive approach was

to use provided brain mask from HCP to make the dense time series and try to mask it with the dense label file during parcellation. The dense label file and dense time series were in their original volume spaces. This resulted in a prompt that stated that the time series and the label file were in different volume spaces. This problem was fixed by using an affine transformation on the mask to fit the data described in Section 5.3.1 about creating the dense label file. Even after matching the voxel size, the naive approach of using the brain mask from HCP had its problems. The atlas has voxels in some areas that the brain mask does not. This can be seen in Figure 6.6. This figure shows that the brain mask has a voxel value of 0, indicating that the voxel is not included when creating a dense time series. However, if the dense time series is masked with the atlas mask, the value of the same voxel is set to 0 in the dense time series, as shown by the highlighted text in Figure 6.7. It is therefore included and has not been omitted.

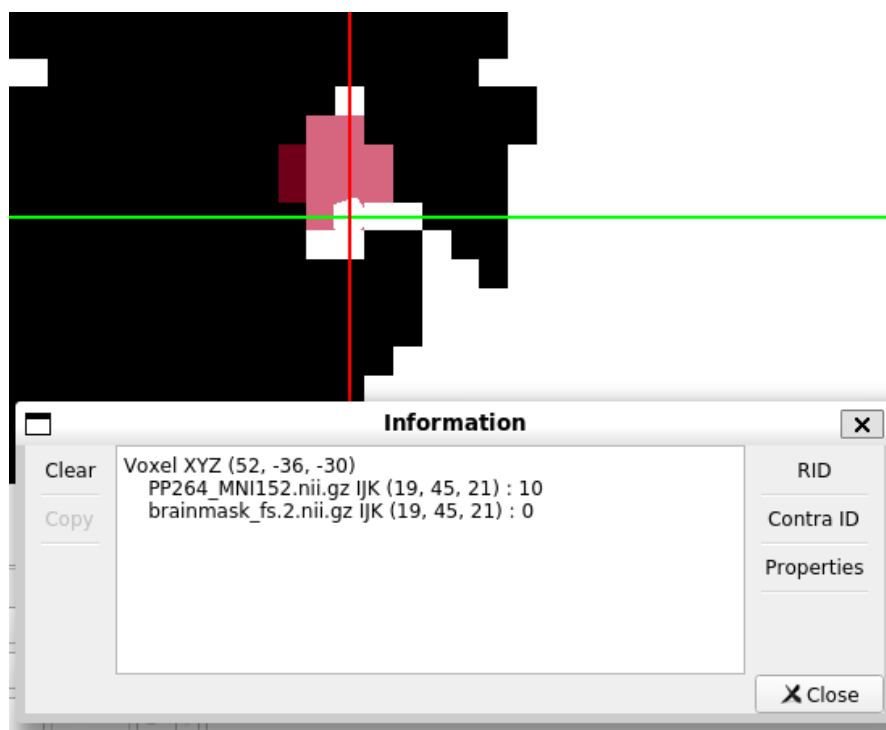


Figure 6.6: Demonstration of missing voxel compared to atlas mask. The black area represents the binary mask of the brain. The light red cross represents the affine-transformed Power et al. mask. The crosshair highlights a voxel included in the Power et al. atlas but not in the brain mask.

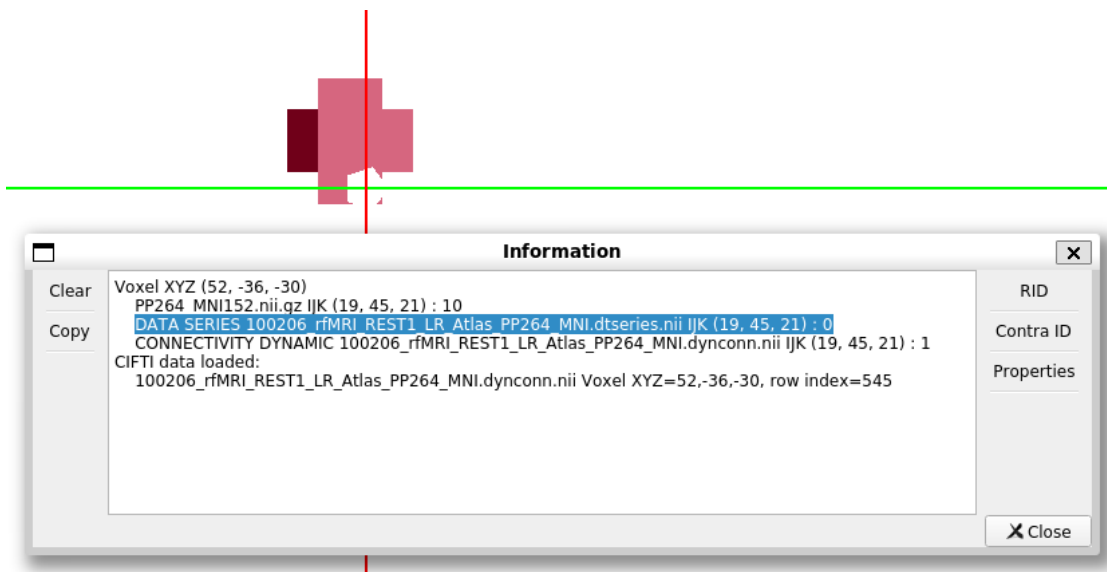


Figure 6.7: The figure shows a dense time series masked with the affine-transformed Power et al. atlas during its creation. The darker red area coincides with the area included in the brain mask. The lighter red area is not a part of the brain mask, but when the dense time series is created with the Power et al. mask, the voxels not included in the brain mask but a part of the Power et al. mask is set to 0.

DPABI Toolbox

It was difficult to find information about some functions in DPABI. For instance, *bounding box* is a function used for normalization. Information about this function can be found in the SPM12 manual [102]. However, it has not been explained in detail in the manual. Therefore, we used the default value. The default mask was also a function that did not have sufficient documentation. The information we found was one sentence on a forum [103] and a PowerPoint [98] provided by the creator of the DPABI. AutoMask was another function which was difficult to find any information about. The information we gathered was from a YouTube video about DSPARF [96] provided by associate Professor Lu and the PowerPoint provided by the creator of the DPABI. The Affine regularisation in the segmentation function was set to European. The option was between East Asian and European. We assumed that most of the subjects were European.

Based on the recommended range for smoothing in Section 2.5.9, the kernel should be within 4 mm to 6 mm, corresponding to 2 to 3 times the voxel size of 2 mm. However, we opted for an 8 mm kernel size due to its widespread use in the fMRI literature and its default value in SPM [99]. The choice of an 8 mm kernel size could have led to excessive spatial smoothing, potentially resulting in augmented functional connectivity. The overt smoothing may have formed connections by blending nearby regions, even if they don't belong to the same nodes/networks.

One of the driving factors for doing a qualitative study was the processing time when using DPABI. The preprocessing and resting state analysis took 28 hours for one subject. Therefore a qualitative approach was more suitable as a greater learning experience as an introduction to the field of neuroscience. This, however, results in a study that does not give any validity to the general population of healthy young adults.

Metric Analyses

The metric analyses were performed on the Pearson correlated matrices, not the Fisher R-to-Z-transformed matrices. This was done due to using SSIM and UQI as similarity metrics. The metrics are calculated using sliding windows, as described in Section 2.7. Using the generated functional connectivity matrices after Fisher R-to-Z transforms would result in similarity indexes of either NaN (not a number) or ∞ because of the diagonal elements. When replacing the diagonal elements with values significantly higher than the off-diagonal elements, the SSIM and UQI values change based on the chosen value. Due to the sliding windows calculation of the metrics, using the upper or lower triangles of the matrices would not work, resulting in errors. It would be preferable to use a metric where this would be possible since it would be possible to calculate the similarity of one of the triangles and omit the diagonal. This approach would likely have

more difficulty comparing spatial information if the matrices are flattened to a column or row vector.

Function Connectivity Matrix

The functional connectivity matrix shown in Figure 6.1 does not specify each node according to the Power et al. atlas template from Table 2.1. The default mode network shown in Figure 6.1 is simplified. The default mode network is highlighted as shown in Figure 6.8. In the highlighted area, it can be observed that most of it consist of default mode network nodes, but some uncertain nodes, memory retrieval nodes and a ventral attention node are also present. The simplification is done to get a better overview of the nodes.

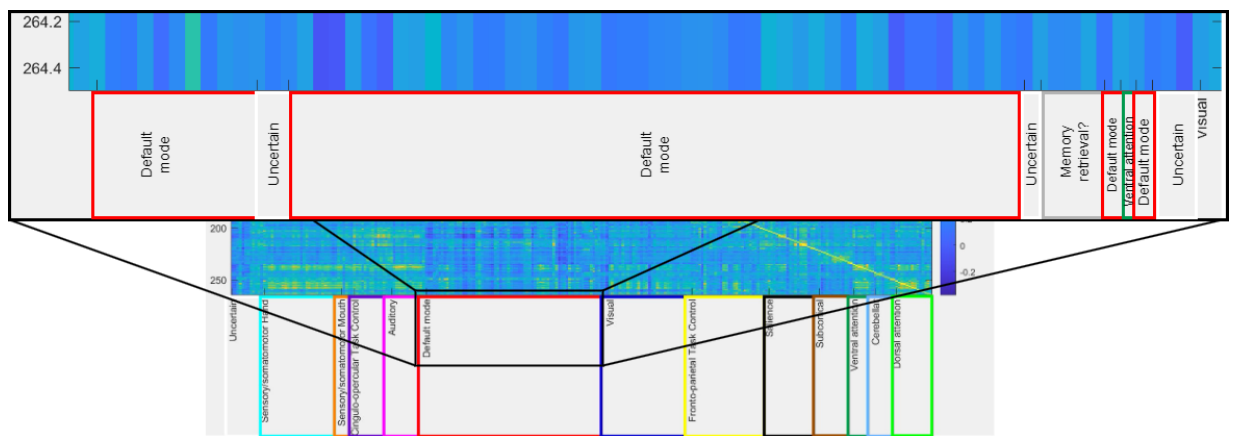


Figure 6.8: A zoomed view of Figure 6.1, which highlights the composition of the default mode region

Chapter 7

Conclusion

This study aimed to provide an introductory resource in the field of neuroimaging, explicitly focusing on volume-based analysis for generating functional connectivity matrices. Two experiments explored the patterns and relationships of brain regions in resting state data. Experiment one compared the functional connectivity matrix produced using DPABI preprocessing and resting state analysis on HCP raw data with the matrix produced using Workbench to perform resting state analysis on DPABI preprocessed data. Experiment two compared the functional connectivity matrix produced using DPABI with the matrix created utilising the Workbench to perform resting state analysis on HCP preprocessed data.

The result of experiment one is that the produced matrices had no noticeable differences by visual inspection. The similarity metrics also support this statement. Experiment two resulted in two matrices with noticeable differences where the structure was similar but with different overall intensities. The similarity metrics also reflected the differences between the matrices with lower values. The calculated mean difference between the matrix elements was 0.327.

The findings of this study indicated that preprocessing techniques impacted the subject's functional connectivity matrices. These observations highlight the importance of selecting appropriate preprocessing methods when performing resting state analysis. Further research is warranted to better understand the specific preprocessing steps that optimise functional connectivity analyses. The study should also be conducted with more subjects such that a statistical analysis may be conducted with more validity for the general population of healthy young adults.

Appendix A

Poster

Bibliography

- [1] Omid Kardan, Sydney Kaplan, Muriah D. Wheelock, Eric Feczko, Trevor K. M. Day, Óscar Miranda-Domínguez, Dominique Meyer, Adam T. Eggebrecht, Lucille A. Moore, Sooyeon Sung, Taylor A. Chamberlain, Eric Earl, Kathy Snider, Alice Graham, Marc G. Berman, Kamil Uğurbil, Essa Yacoub, Jed T. Elison, Christopher D. Smyser, Damien A. Fair, and Monica D. Rosenberg. Resting-state functional connectivity identifies individuals and predicts age in 8-to-26-month-olds. *Developmental Cognitive Neuroscience*, 56:101123, August 2022. ISSN 1878-9293. doi: 10.1016/j.dcn.2022.101123.
- [2] Deanna M. Barch. Resting State Functional Connectivity in the Human Connectome Project: Current Status and Relevance to Understanding Psychopathology. *Harvard review of psychiatry*, 25(5):209–217, September 2017. doi: 10.1097/HRP.000000000000166.
- [3] Jonathan D. Power, Damien A. Fair, Bradley L. Schlaggar, and Steven E. Petersen. The Development of Human Functional Brain Networks. *Neuron*, 67(5):735–748, September 2010. ISSN 0896-6273. doi: 10.1016/j.neuron.2010.08.017. URL <https://www.sciencedirect.com/science/article/pii/S0896627310006276>. [Accessed: 2023-05-29].
- [4] Gabriella V. Hirsch, Corinna M. Bauer, and Lotfi B. Merabet. Using structural and functional brain imaging to uncover how the brain adapts to blindness. *Annals of neuroscience and psychology*, 2:5, Aug 2015. URL <https://www.ncbi.nlm.nih.gov/pmc/articles/PMC6168211/>.
- [5] Prof Joanna Wardlaw. Structural mr. *The University of Edinburgh*, Jun 2021. URL <https://www.ed.ac.uk/clinical-sciences/edinburgh-imaging/research/themes-and-topics/medical-physics/imaging-techniques/structural-mr>.
- [6] Daisuke Kawahara and Yasushi Nagata. T1-weighted and T2-weighted MRI image synthesis with convolutional generative adversarial networks. *Reports of Practical Oncology and Radiotherapy*, 26(1):35, 2021. doi: 10.5603/RPOR.a2021.0005.

- [7] Simon S. Keller¹ and Neil Roberts². Measurement of brain volume using mri: software, techniques, choices and prerequisites. *Journal of Anthropological Sciences*, 87:127–151, 2009. URL https://www.isita-org.com/jass/contents/2009%20vol87/pdf/on-line_bassa/jass2009_05_keller.pdf.
- [8] Ian B. Malone, Kelvin K. Leung, Shona Clegg, Josephine Barnes, Jennifer L. Whitwell, John Ashburner, Nick C. Fox, and Gerard R. Ridgway. Accurate automatic estimation of total intracranial volume: A nuisance variable with less nuisance. *Neuroimage*, 104:366, January 2015. doi: 10.1016/j.neuroimage.2014.09.034.
- [9] All About Functional Magnetic Resonance Imaging (fMRI), December 2021. URL <https://psychcentral.com/lib/what-is-functional-magnetic-resonance-imaging-fmri#uses>. [Accessed: 2023-03-27].
- [10] Maksim G. Sharaev, Viktoria V. Zavyalova, Vadim L. Ushakov, Sergey I. Kartashov, and Boris M. Velichkovsky. Effective Connectivity within the Default Mode Network: Dynamic Causal Modeling of Resting-State fMRI Data. *Frontiers in Human Neuroscience*, 10, February 2016. ISSN 1662-5161. doi: 10.3389/fnhum.2016.00014.
- [11] H. Lv, Z. Wang, E. Tong, L. M. Williams, G. Zaharchuk, M. Zeineh, A. N. Goldstein-Piekarski, T. M. Ball, C. Liao, and M. Wintermark. Resting-State Functional MRI: Everything That Nonexperts Have Always Wanted to Know. *AJNR: American Journal of Neuroradiology*, 39(8):1390–1399, August 2018. doi: 10.3174/ajnr.A5527.
- [12] Neuroimaging Research Methods. Resting state functional connectivity: Part 1 - introduction, 2019. URL https://www.youtube.com/watch?v=5yDN2q7gUaM&t=21s&ab_channel=NeuroimagingResearchMethods.
- [13] Ph.D Catie Chang. Ismrm mr academy: "dynamic functional connectivity", 2021. URL https://www.youtube.com/watch?v=QwAYwxpNUFA&t=1547s&ab_channel=ISMRRM-ISMRT.
- [14] InjuryMap. Medical illustration of the human brain seen from the side., April 25, 2019. URL <https://www.injurymap.com/free-human-anatomy-illustrations>. This work is licensed under the Creative Commons Attribution 4.0 International License. To view a copy of this license, visit <https://creativecommons.org/licenses/by-sa/4.0/deed.en/>. [Accessed: 2023-04-21], via Wikimedia Commons.

- [15] Dustin Scheinost, Rajita Sinha, Sarah Cross, Soo Hyun Kwon, Gordon Sze, Robert Constable, and Laura Ment. Does prenatal stress alter the developing connectome? *Pediatric research*, 81, 09 2016. doi: 10.1038/pr.2016.197.
- [16] Jessica R. Andrews-Hanna, Jay S. Reidler, Jorge Sepulcre, Renee Poulin, and Randy L. Buckner. Functional-anatomic fractionation of the brain's default network. *Neuron*, 65(4):550–562, 2010. ISSN 0896-6273. doi: <https://doi.org/10.1016/j.neuron.2010.02.005>. URL <https://www.sciencedirect.com/science/article/pii/S0896627310000966>.
- [17] Alex Fornito, Andrew Zalesky, and Edward T. Bullmore. Chapter 3 - connectivity matrices and brain graphs. In *Fundamentals of Brain Network Analysis*, pages 89–113. Academic Press, San Diego, 2016. ISBN 978-0-12-407908-3. doi: <https://doi.org/10.1016/B978-0-12-407908-3.00003-0>. URL <https://www.sciencedirect.com/science/article/pii/B9780124079083000030>.
- [18] Demonstrational Data for Resting-State fMRI, May 2021. URL <http://rfmri.org/DemoData>. [Accessed 2023-06-10].
- [19] Lei Wu, Arvind Caprihan, Juan Bustillo, Andrew Mayer, and Vince Calhoun. An approach to directly link ICA and seed-based functional connectivity: application to schizophrenia. *NeuroImage*, 179:448, October 2018. doi: 10.1016/j.neuroimage.2018.06.024.
- [20] William Sohn, Kwangsun Yoo, Young-Beom Lee, Sang Seo, Duk Na, and Yong Jeong. Influence of roi selection on resting state functional connectivity: an individualized approach for resting state fmri analysis. *Frontiers in Neuroscience*, 9, 2015. ISSN 1662-453X. doi: 10.3389/fnins.2015.00280. URL <https://www.frontiersin.org/articles/10.3389/fnins.2015.00280>.
- [21] Lingzhong Fan, Hai Li, Junjie Zhuo, Yu Zhang, Jiaojian Wang, Liangfu Chen, Zhengyi Yang, Congying Chu, Sangma Xie, Angela R. Laird, Peter T. Fox, Simon B. Eickhoff, Chunshui Yu, and Tianzi Jiang. The human brainnetome atlas: A new brain atlas based on connectional architecture. *Cerebral cortex*, 2016. ISSN 3508–3526. doi: <https://doi.org/10.1093/cercor/bhw157>. URL <https://www.ncbi.nlm.nih.gov/pmc/articles/PMC4961028/>.
- [22] Jonathan D. Power, Alexander L. Cohen, Steven M. Nelson, Gagan S. Wig, Kelly Anne Barnes, Jessica A. Church, Alecia C. Vogel, Timothy O. Laumann, Fran M. Miezin, Bradley L. Schlaggar, and Steven E. Petersen. Functional network organization of the human brain. *Neuron*, 72(4):665–678, 2011. ISSN 0896-6273. doi: <https://doi.org/10.1016/j.neuron.2011.09.006>. URL <https://www.sciencedirect.com/science/article/pii/S0896627311007926>.

- [23] Sneha Chenji, Shankar Jha, Dawon Lee, Matthew Brown, Peter Seres, Dennell Mah, and Sanjay Kalra. Investigating default mode and sensorimotor network connectivity in amyotrophic lateral sclerosis. *PLOS ONE*, 11(6):1–14, 06 2016. doi: 10.1371/journal.pone.0157443. URL <https://doi.org/10.1371/journal.pone.0157443>.
- [24] Caterina Gratton, Ally Dworetzky, Babatunde Adeyemo, Benjamin A. Seitzman, Derek M. Smith, Steven E. Petersen, and Mital Neta. The cingulo-opercular network is composed of two distinct sub-systems. *bioRxiv*, 2022. doi: 10.1101/2022.09.16.508254. URL <https://www.biorxiv.org/content/early/2022/09/18/2022.09.16.508254>.
- [25] R.S. Lockhart. Memory retrieval. In Neil J. Smelser and Paul B. Baltes, editors, *International Encyclopedia of the Social & Behavioral Sciences*, pages 9613–9618. Pergamon, Oxford, 2001. ISBN 978-0-08-043076-8. doi: <https://doi.org/10.1016/B0-08-043076-7/01523-0>. URL <https://www.sciencedirect.com/science/article/pii/B0080430767015230>.
- [26] Simone Vossel, Joy J. Geng, and Gereon R. Fink. Dorsal and Ventral Attention Systems: Distinct Neural Circuits but Collaborative Roles. *Neuroscientist*, 20(2): 150, April 2014. doi: 10.1177/1073858413494269.
- [27] Jakub Schimmelpfennig, Jan Topczewski, Wojciech Zajkowski, and Kamila Jankowiak-Siuda. The role of the salience network in cognitive and affective deficits. *Frontiers in Human Neuroscience*, 17, 2023. ISSN 1662-5161. doi: 10.3389/fnhum.2023.1133367. URL <https://www.frontiersin.org/articles/10.3389/fnhum.2023.1133367>.
- [28] Jana Vasković M. D. Subcortical structures. *Kenhub*, April 2023. URL <https://www.kenhub.com/en/library/anatomy/subcortical-structures-anatomy>.
- [29] Egidio D’Angelo. The cerebellar network: revisiting the critical issues. *Journal of Physiology*, 589(Pt 14):3421, July 2011. doi: 10.1113/jphysiol.2011.213496.
- [30] Russell A. Poldrack, Jeanette A. Mumford, and Thomas E. Nichols. *Spatial normalization*, page 53–69. Cambridge University Press, 2011. doi: 10.1017/CBO9780511895029.005.
- [31] Chaogan Yan and Yufeng Zang. Dparsf: a matlab toolbox for "pipeline" data analysis of resting-state fmri. *Frontiers in Systems Neuroscience*, 4, 2010. ISSN 1662-5137. doi: 10.3389/fnsys.2010.00013. URL <https://www.frontiersin.org/articles/10.3389/fnsys.2010.00013>.

- [32] Ronald Sladky, Karl J. Friston, Jasmin Tröstl, Ross Cunnington, Ewald Moser, and Christian Windischberger. Slice-timing effects and their correction in functional mri. *NeuroImage*, 58(2):588–594, 2011. ISSN 1053-8119. doi: <https://doi.org/10.1016/j.neuroimage.2011.06.078>. URL <https://www.sciencedirect.com/science/article/pii/S1053811911007245>.
- [33] David B. Parker and Qolamreza R. Razlighi. The benefit of slice timing correction in common fmri preprocessing pipelines. *Frontiers in Neuroscience*, 13, 2019. ISSN 1662-453X. doi: 10.3389/fnins.2019.00821. URL <https://www.frontiersin.org/articles/10.3389/fnins.2019.00821>.
- [34] Raheel Zafar, Aamir Malik, Nidal Kamel, and Sarat Dass. Importance of realignment parameters in fmri data analysis. *Conference: 2015 IEEE International Conference on Signal and Image Processing Applications (ICSIPA)*, pages 546–550, 10 2015. doi: 10.1109/ICSIPA.2015.7412251.
- [35] Enzo Ferrante and Nikos Paragios. Slice-to-volume medical image registration: A survey. *Medical Image Analysis*, 39, 02 2017. doi: 10.1016/j.media.2017.04.010.
- [36] Junchen Wang, Zhen Sun, Honglei Ji, Xiaohui Zhang, Tianmiao Wang, and Yu Shen. A fast 3d brain extraction and visualization framework using active contour and modern opengl pipelines. *IEEE Access*, PP:1–1, 10 2019. doi: 10.1109/ACCESS.2019.2948621.
- [37] Stephen M. Smith, Mark Jenkinson, Mark W. Woolrich, Christian F. Beckmann, Timothy E.J. Behrens, Heidi Johansen-Berg, Peter R. Bannister, Marilena De Luca, Ivana Drobnjak, David E. Flitney, Rami K. Niazy, James Saunders, John Vickers, Yongyue Zhang, Nicola De Stefano, J. Michael Brady, and Paul M. Matthews. Advances in functional and structural mr image analysis and implementation as fsl. *NeuroImage*, 23:S208–S219, 2004. ISSN 1053-8119. doi: <https://doi.org/10.1016/j.neuroimage.2004.07.051>. URL <https://www.sciencedirect.com/science/article/pii/S1053811904003933>. Mathematics in Brain Imaging.
- [38] Stephen M. Smith. Fast robust automated brain extraction. *Human Brain Mapping*, 17(3):143–155, 2002. doi: <https://doi.org/10.1002/hbm.10062>. URL <https://onlinelibrary.wiley.com/doi/abs/10.1002/hbm.10062>.
- [39] Mark Jenkinson. Image registration and motion correction, [Accessed: 2023-04-20]. URL https://afni.nimh.nih.gov/sscc/staff/rwcox/ISMRM_2006/Syllabus%202006%20-%203340/files/B_05.pdf.
- [40] Dongha Lee, Changwon Jang, and Hae-Jeong Park. Multivariate detrending of fmri signal drifts for real-time multiclass pattern classification. *NeuroImage*, 108:203–213,

2015. ISSN 1053-8119. doi: <https://doi.org/10.1016/j.neuroimage.2014.12.062>. URL <https://www.sciencedirect.com/science/article/pii/S1053811914010672>.
- [41] Chao-Gan Yan, Brian Cheung, Clare Kelly, Stan Colcombe, R. Cameron Craddock, Adriana Di Martino, Qingyang Li, Xi-Nian Zuo, F. Xavier Castellanos, and Michael P. Milham. A comprehensive assessment of regional variation in the impact of head micromovements on functional connectomics. *NeuroImage*, 76:183–201, 2013. ISSN 1053-8119. doi: <https://doi.org/10.1016/j.neuroimage.2013.03.004>. URL <https://www.sciencedirect.com/science/article/pii/S1053811913002127>.
- [42] Jonathan D. Power, Kelly Anne Barnes, Abraham Z. Snyder, Bradley L. Schlaggar, and Steven E. Petersen. Steps toward optimizing motion artifact removal in functional connectivity MRI; a reply to Carp. *NeuroImage*, 76, August 2013. doi: [10.1016/j.neuroimage.2012.03.017](https://doi.org/10.1016/j.neuroimage.2012.03.017).
- [43] Jonathan D. Power, Kelly A. Barnes, Abraham Z. Snyder, Bradley L. Schlaggar, and Steven E. Petersen. Spurious but systematic correlations in functional connectivity mri networks arise from subject motion. *NeuroImage*, 59(3):2142–2154, 2012. ISSN 1053-8119. doi: <https://doi.org/10.1016/j.neuroimage.2011.10.018>. URL <https://www.sciencedirect.com/science/article/pii/S1053811911011815>.
- [44] Theodore D. Satterthwaite, Daniel H. Wolf, James Loughhead, Kosha Ruparel, Mark A. Elliott, Hakon Hakonarson, Ruben C. Gur, and Raquel E. Gur. Impact of in-scanner head motion on multiple measures of functional connectivity: Relevance for studies of neurodevelopment in youth. *NeuroImage*, 60(1):623–632, 2012. ISSN 1053-8119. doi: <https://doi.org/10.1016/j.neuroimage.2011.12.063>. URL <https://www.sciencedirect.com/science/article/pii/S1053811911014650>.
- [45] Koene R.A. Van Dijk, Mert R. Sabuncu, and Randy L. Buckner. The influence of head motion on intrinsic functional connectivity mri. *NeuroImage*, 59(1):431–438, 2012. ISSN 1053-8119. doi: <https://doi.org/10.1016/j.neuroimage.2011.07.044>. URL <https://www.sciencedirect.com/science/article/pii/S1053811911008214>. Neuroergonomics: The human brain in action and at work.
- [46] Karl J. Friston, Steven Williams, Robert Howard, Richard S. J. Frackowiak, and Robert Turner. Movement-related effects in fmri time-series. *Magnetic Resonance in Medicine*, 35(3):346–355, 1996. doi: <https://doi.org/10.1002/mrm.1910350312>. URL <https://onlinelibrary.wiley.com/doi/abs/10.1002/mrm.1910350312>.
- [47] Lars Kasper, Steffen Bollmann, Andreea O. Diaconescu, Chloe Hutton, Jakob Heinzle, Sandra Iglesias, Tobias U. Hauser, Miriam Sebold, Zina-Mary Manjaly, Klaas P. Pruessmann, and Klaas E. Stephan. The physio toolbox for modeling

- physiological noise in fmri data. *Journal of Neuroscience Methods*, 276:56–72, 2017. ISSN 0165-0270. doi: <https://doi.org/10.1016/j.jneumeth.2016.10.019>. URL <https://www.sciencedirect.com/science/article/pii/S016502701630259X>.
- [48] Jonathan Brooks, Olivia Faull, Kyle Pattinson, and Mark Jenkinson. Physiological noise in brainstem fmri. *Frontiers in Human Neuroscience*, 7, 2013. ISSN 1662-5161. doi: 10.3389/fnhum.2013.00623. URL <https://www.frontiersin.org/articles/10.3389/fnhum.2013.00623>.
- [49] Alican Nalci, Bhaskar D. Rao, and Thomas T. Liu. Nuisance effects and the limitations of nuisance regression in dynamic functional connectivity fmri. *NeuroImage*, 184:1005–1031, 2019. ISSN 1053-8119. doi: <https://doi.org/10.1016/j.neuroimage.2018.09.024>. URL <https://www.sciencedirect.com/science/article/pii/S1053811918308097>.
- [50] David M. Lydon-Staley, Rastko Ciric, Theodore D. Satterthwaite, and Danielle S. Bassett. Evaluation of confound regression strategies for the mitigation of micromovement artifact in studies of dynamic resting-state functional connectivity and multilayer network modularity. *Network Neuroscience*, 3(2):427, 2019. doi: 10.1162/netn_a_00071.
- [51] Jenny Crinion, John Ashburner, Alex Leff, Matthew Brett, Cathy Price, and Karl Friston. Spatial normalization of lesioned brains: Performance evaluation and impact on fmri analyses. *NeuroImage*, 37(3):866–875, 2007. ISSN 1053-8119. doi: <https://doi.org/10.1016/j.neuroimage.2007.04.065>. URL <https://www.sciencedirect.com/science/article/pii/S1053811907003266>.
- [52] John Ashburner. A fast diffeomorphic image registration algorithm. *NeuroImage*, 38(1):95–113, 2007. ISSN 1053-8119. doi: <https://doi.org/10.1016/j.neuroimage.2007.07.007>. URL <https://www.sciencedirect.com/science/article/pii/S1053811907005848>.
- [53] Wanjie Tang, Bin Li, Xiaoqi Huang, Xiaoyu Jiang, Fei Li, Lijuan Wang, Taolin Chen, Jinhui Wang, Qiyong Gong, and Yanchun Yang. Morphometric brain characterization of refractory obsessive–compulsive disorder: Diffeomorphic anatomic registration using exponentiated lie algebra. *Progress in Neuro-Psychopharmacology and Biological Psychiatry*, 46:126–131, 2013. ISSN 0278-5846. doi: <https://doi.org/10.1016/j.pnpbp.2013.07.011>. URL <https://www.sciencedirect.com/science/article/pii/S0278584613001528>.
- [54] P. Ripollés, J. Marco-Pallarés, R. de Diego-Balaguer, J. Miró, M. Falip, M. Juncadella, F. Rubio, and A. Rodriguez-Fornells. Analysis of automated methods

- for spatial normalization of lesioned brains. *NeuroImage*, 60(2):1296–1306, 2012. ISSN 1053-8119. doi: <https://doi.org/10.1016/j.neuroimage.2012.01.094>. URL <https://www.sciencedirect.com/science/article/pii/S1053811912001115>.
- [55] Alexis Giff, Georg Noren, John Magnotti, Antonio Carlos Lopes, Marcelo Camargo Batistuzzo, Marcelo Hoexter, Benjamin Greenberg, Richard Marsland, Euripedes Constantino Miguel, Steven Rasmussen, and Nicole McLaughlin. Spatial normalization discrepancies between native and MNI152 brain template scans in gamma ventral capsulotomy patients. *Psychiatry Research: Neuroimaging*, 329: 111595, March 2023. ISSN 0925-4927. doi: 10.1016/j.psychres.2023.111595.
- [56] NITRC: Automated Image Registration (AIR): Tool/Resource Info, May 2023. URL <https://www.nitrc.org/projects/air>. [Accessed:2023-05-24].
- [57] Pravat K. Mandal, Rashima Mahajan, and Ivo D. Dinov. Structural Brain Atlases: Design, Rationale, and Applications in Normal and Pathological Cohorts. *Journal of Alzheimer's disease : JAD*, 31(0 3):S169, 2012. doi: 10.3233/JAD-2012-120412.
- [58] Michal Mikl, Radek Mareček, Petr Hlušík, Martina Pavlicová, Aleš Drastich, Pavel Chlebus, Milan Brázdil, and Petr Krupa. Effects of spatial smoothing on fmri group inferences. *Magnetic Resonance Imaging*, 26(4):490–503, 2008. ISSN 0730-725X. doi: <https://doi.org/10.1016/j.mri.2007.08.006>. URL <https://www.sciencedirect.com/science/article/pii/S0730725X07003955>.
- [59] Arne Nordmann (norro), November, 2007. URL <https://commons.wikimedia.org/wiki/File:FWMH.svg>. This work is licensed under the Creative Commons Attribution 3.0 International License. To view a copy of this license, visit <https://creativecommons.org/licenses/by-sa/3.0/deed.en>. [Accessed: 2023-05-15], via Wikimedia Commons.
- [60] Marta Moraschi, Gisela E. Hagberg, Margherita Di Paola, Gianfranco Spalletta, Bruno Maraviglia, and Federico Giove. Smoothing that does not blur: Effects of the anisotropic approach for evaluating diffusion tensor imaging data in the clinic. *Journal of Magnetic Resonance Imaging*, 31(3):690–697, 2010. doi: <https://doi.org/10.1002/jmri.22040>. URL <https://onlinelibrary.wiley.com/doi/abs/10.1002/jmri.22040>.
- [61] Shogo Kajimura, Daniel Margulies, and Jonathan Smallwood. Frequency-specific brain network architecture in resting-state fMRI. *Scientific Reports*, 13(2964):1–9, February 2023. ISSN 2045-2322. doi: 10.1038/s41598-023-29321-5.
- [62] Zhijun Yao, Bin Hu, Yuanwei Xie, Philip Moore, and Jiaxiang Zheng. A review of structural and functional brain networks: small world and atlas.

- Brain Informatics*, 2:45–52, 2015. ISSN 2198-4026. doi: <https://doi.org/10.1007/s40708-015-0009-z>. URL <https://braininformatics.springeropen.com/articles/10.1007/s40708-015-0009-z>.
- [63] Dietmar Cordes, Victor M. Haughton, Konstantinos Arfanakis, Gary J. Wendt, Patrick A. Turski, Chad H. Moritz, Michelle A. Quigley, and M. Elizabeth Meyerand. Mapping functionally related regions of brain with functional connectivity mr imaging. *American Journal of Neuroradiology*, 21(9):1636–1644, 2000.
- [64] Peter Fransson. Spontaneous low-frequency BOLD signal fluctuations: An fMRI investigation of the resting-state default mode of brain function hypothesis. *Human Brain Mapping*, 26(1):15, September 2005. doi: 10.1002/hbm.20113.
- [65] John Bates. Correlation analysis, 2021. URL <https://business.adobe.com/blog/basics/correlation-analysis>.
- [66] Michael W. Cole, Genevieve J. Yang, John D. Murray, Grega Repovš, and Alan Anticevic. Functional connectivity change as shared signal dynamics. *Journal of Neuroscience Methods*, 259:22–39, 2016. ISSN 0165-0270. doi: <https://doi.org/10.1016/j.jneumeth.2015.11.011>. URL <https://www.sciencedirect.com/science/article/pii/S0165027015004136>.
- [67] Arun S. Mahadevan, Ursula A. Tooley, Maxwell A. Bertolero, Allyson P. Mackey, and Danielle S. Bassett. Evaluating the sensitivity of functional connectivity measures to motion artifact in resting-state fmri data. *NeuroImage*, 241:118408, 2021. ISSN 1053-8119. doi: <https://doi.org/10.1016/j.neuroimage.2021.118408>. URL <https://www.sciencedirect.com/science/article/pii/S1053811921006832>.
- [68] Ph.D. Naomi J. Goodrich-Hunsaker. Functional connectivity, [Accessed: 2023-04-05]. URL <https://bookdown.org/u0243256/tbicc/functional-connectivity.html>.
- [69] Diva Jain. Relationship_between_mean_and_median_under_different_skewness, August 23 2018. URL <https://codeburst.io/2-important-statistics-terms-you-need-to-know-in-data-science-skewness-and-kurt>. This work is licensed under the Creative Commons Attribution 4.0 International License. To view a copy of this license, visit <https://creativecommons.org/licenses/by-sa/4.0/deed.en/>. [Accessed: 2023-05-21], via Wikimedia Commons.
- [70] Ken Stewart. Mean squared error (MSE) | Definition, Formula, Interpretation, & Facts. *Encyclopedia Britannica*, March 2023. URL <https://www.britannica.com/science/mean-squared-error>.

- [71] Jim Frost. Mean Squared Error (MSE). *Statistics By Jim*, May 2023. URL <https://statisticsbyjim.com/regression/mean-squared-error-mse>.
- [72] Zhou Wang and A. C. Bovik. A universal image quality index. *IEEE Signal Processing Letters*, 9(3):81–84, March 2002. ISSN 1558-2361. doi: 10.1109/97.995823.
- [73] Zhou Wang, A.C. Bovik, H.R. Sheikh, and E.P. Simoncelli. Image quality assessment: from error visibility to structural similarity. *IEEE Transactions on Image Processing*, 13(4):600–612, 2004. doi: 10.1109/TIP.2003.819861.
- [74] Michael Moore, Brandon Patterson, Sara Samuel, Helenmary Sheridan, and Chris Sorensen. *Neuroimaging DICOM and NIfTI Data Curation Primer*. Data Curation Network, 2020. URL <http://hdl.handle.net/11299/216582>.
- [75] Mark Jenkinson. Nifti-2: a 64-bit update of nifti1 (approved). NITRC, Mar 2011. URL https://www.nitrc.org/forum/forum.php?thread_id=2148&forum_id=1941. [Accessed: 2023-5-15].
- [76] NITRC. *cifti:Cifti-1*, Last updated: May 2014. URL <https://www.nitrc.org/plugins/mwiki/index.php?title=cifti:Cifti-1>. [Accessed: 2023-5-16].
- [77] Tim Coalson, Matt Glasser, John Harwell, David Van Essen, Mark Jenkinson, and Robert Oostenveld. *CIFTI-2 Connectivity File Formats Documentation CIFTI working group*, Mar 2014.
- [78] What is XML, May 2023. URL <https://aws.amazon.com/what-is/xml>. [Accessed: 2023-05-04].
- [79] Connectome Coordinate Facility, May 2023. URL <https://www.humanconnectome.org>. [Accessed: 2023-05-19].
- [80] National Institute of Mental Health. Human connectome project (hcp), 2022. URL <https://www.nimh.nih.gov/research/research-funded-by-nimh/research-initiatives/human-connectome-project-hcp>.
- [81] HCP Young Adults:1200 Subjects Data Release, March 2017. URL <https://www.humanconnectome.org/study/hcp-young-adult/document/1200-subjects-data-release>. [Accessed: 2023-05-19].
- [82] *WU-Minn HCP 1200 Subjects Release: Reference Manual*. Human Connectome Project, March 2017. URL https://www.humanconnectome.org/storage/app/media/documentation/s1200/HCP_S1200_Release_Appendix_I.pdf.

- [83] Jaber Juntu, Jan Sijbers, Dirk Van Dyck, and Jan Gielen. Bias Field Correction for MRI Images. In *Computer Recognition Systems*, pages 543–551. Springer, Berlin, Germany, 2005. doi: 10.1007/3-540-32390-2_64.
- [84] Chao-Gan Yan, Xin-Di Wang, Xi-Nian Zuo, and Yu-Feng Zan. Data Processing Assistant for Resting-State fMRI (DPARSF), January 2022. URL <http://rfmri.org/DPARSF>. [Accessed 2023-06-10].
- [85] SPM - Statistical Parametric Mapping, May 2023. URL <https://www.fil.ion.ucl.ac.uk/spm>. [Accessed 2023-06-10].
- [86] Chao-Gan Yan, Xin-Di Wang, Xi-Nian Zuo, and Yu-Feng Zan. DPABI: a toolbox for Data Processing & Analysis for Brain Imaging, March 2023. URL <http://rfmri.org/DPABI>. [Accessed 2023-06-10].
- [87] Chao-Gan Yan, Xin-Di Wang, Xi-Nian Zuo, and Yu-Feng Zang. DPABI: Data Processing & Analysis for (Resting-State) Brain Imaging. *Neuroinformatics*, 14(3): 339–351, July 2016. ISSN 1559-0089. doi: 10.1007/s12021-016-9299-4.
- [88] Ph.D Chao-Gan Yan. Resting-state fmri: Principles of data processing and introduction to dparsec, 2016. URL https://rfmri.org/WebinarCourse_20160125.
- [89] craigloewen msft, NotTheDr01ds, alexbuckgit, mattwojo, Aaron-Junker, DrInfiniteExplorer, v chmcl, and v surgos. Frequently asked questions about windows subsystem for linux, 2023. URL <https://learn.microsoft.com/en-us/windows/wsl/faq>. [Accessed: 2023-03-05].
- [90] craigloewen msft, mattwojo, donwilson, wibjorn, dix, crramirez, pzhlkj6612, and v alje. Install linux on windows with wsl, 2023. URL <https://learn.microsoft.com/en-us/windows/wsl/install>. [Accessed: 2023-03-05].
- [91] Bruce Fischl. FreeSurfer. *NeuroImage*, 62(2):774–781, August 2012. ISSN 1053-8119. doi: 10.1016/j.neuroimage.2012.01.021. URL <https://www.sciencedirect.com/science/article/pii/S1053811912000389?via%3Dihub>.
- [92] buildqa. Freesurfer install on ubuntu 18 running in wsl, [Accessed: 2023-03-05]. URL https://surfer.nmr.mgh.harvard.edu/fswiki/FS7_wsl_ubuntu.
- [93] Index of /pub/dist/freesurfer/7.3.1, June 2023. URL <https://surfer.nmr.mgh.harvard.edu/pub/dist/freesurfer/7.3.1>. [Accessed 2023-06-10].
- [94] Connectome Coordination Facility. Connectome - Using Connectome Workbench, June 2023. URL <https://www.humanconnectome.org/software/connectome-workbench>. [Accessed: 2023-05-25].

- [95] Connectome Coordination Facility. Connectome - Using the ConnectomeDB, June 2023. URL <https://www.humanconnectome.org/software/connectomedb>. [Accessed: 2023-05-25].
- [96] Chia-Feng Lu. Dpabi toolbox - functional connectivity, 2019. URL https://www.youtube.com/watch?v=0IKPii6rIzE&t=841s&ab_channel=AlvinLu4016.
- [97] Descamps, Benedicte and Roggeman, Chantal and Vandemaele, Pieter and Achten, Eric. Image Acquisition Order and Input Order of BOLD-fMRI Data for Slice Time Correction in fMRI Data Processing Tools. In *First Benelux In Vivo MR Methods Symposium 2007 PROGRAM BOOK*, 2007. URL <http://dx.doi.org/1854/10927>.
- [98] Ph.D. Chao-Gan YAN. Data processing of resting-state fmri: Dparsf, 2019. URL http://yanlab.psych.ac.cn/Course/V3.0CN/4_R-fMRI_Data_Processing_DPARSFA.pdf.
- [99] Timothy S. Coalson, David C. Van Essen, and Matthew F. Glasser. The impact of traditional neuroimaging methods on the spatial localization of cortical areas. *Proceedings of the National Academy of Sciences of the United States of America*, 115(27):E6356, July 2018. doi: 10.1073/pnas.1801582115.
- [100] F. Tijhuis, M. Schepers, E. Centeno, B Maciel, de A.P.C., L. Douw, and F. Nobrega Santos. Human connectome project rfMRI repository. san francisco (ca): Github, [Accessed: 2023-3-15]. URL <https://github.com/floristijhuis/HCP-rfMRI-repository>.
- [101] Using workbench command, 2021-02-16. URL <https://www.humanconnectome.org/software/workbench-command>.
- [102] John Ashburner, Gareth Barnes, Chun-Chuan Chen, Jean Daunizeau, Guillaume Flandin, Karl Friston, Darren Gitelman, Volkmar Glauche, Rik Henson, Chloe Hutton, Amirhossein Jafarian, Stefan Kiebel, James Kilner, Vladimir Litvak, Jérémie Mattout, Rosalyn Moran, Will Penny, Christophe Phillips, Adeel Razi, Klaas Stephan, Sungho Tak, Ashley Tyrer, and Peter Zeidman. *SPM12 Manual*. Wellcome Centre for Human Neuroimaging, 2021. URL https://www.fil.ion.ucl.ac.uk/spm/doc/spm12_manual.pdf. [Accessed: 2023-06-01].
- [103] Default mask vs. input mask, October 2013. URL <http://rfmri.org/content/default-mask-vs-input-mask>. [Accessed: 2023-06-5].